Design and Fabrication of a Long-range Surface Plasmon Polariton Wave Guide for near-infrared light

Diplomarbeit

von

Johannes Trapp

Design and Fabrication of a Long-range Surface Plasmon Polariton Wave Guide for near-infrared light

Diplomarbeit

im Studiengang Diplom Physik
der Technischen Universität München

angefertigt an der Fakultät für Physik
der Ludwig-Maximilians-Universität München
Arbeitsgruppe Prof. Dr. Harald Weinfurter

von

Johannes Trapp

München, den 31. Juli 2011

Erstgutachter: Prof. Dr. G. Rempe
Zweitgutachter: Prof. Dr. H. Weinfurter

Acknowledgements

A work like this thesis can of course not be done alone. Accordingly I would like to express my gratitude to the persons who made this thesis possible and contributed to its success.

The first person to thank is Professor Harald Weinfurter, who welcomed me in his group and showed an enormous amount of trust in my endeavours which, in turn, allowed me to work freely. Secondly, great thanks go to Dr. Markus Weber, who explored the world of surface plasmon polaritons with me and always thought of an alternative way to tackle the problems that occurred. Furthermore I would like to thank Philipp Altpeter for his patience to explain to me the variety of machinery and processes in the clean room and who always took the time to help me with his expertise in microfabrication. My office-mate Michael Krug deserves great thanks as well, because he was the first one I turned to for administrative-, computer-, LaTeX- or even smaller problems and he helped without hesitation until the problem was solved. The assistance from Dr. Wenjamin Rosenfeld and Daniel Schlenk should not go unmentioned. They contributed to a smart and sleek experimental setup through productive discussions. Of course my gratitude also goes to my parents as they supported me throughout my studies, not only financially but with good advice and as a source of motivation, as well. Finally, I am very grateful to the wonderful Andrea Wahle, who always cheered me up throughout the long patches of unsuccessful fabrication attempts and then celebrated the successive breakthrough with me.

Thank you all for your support throughout the year.

Contents

1. Introduction

Light has always been used as a mean of communication for mankind. Starting with the ancient Greeks that used fire to pass basic messages like the victory in a battle, light — or the absence thereof — carried information for the people.

Today's modern telecommunication systems, first and foremost the internet, would not be possible without optical data transfer. At long distances the use of light to encode and transmit information is uncontested. Light guided through optical fibres, that rely on the principle of total internal reflection, exhibits very low losses and it has an inherently high data capacity compared to electrical systems. With the establishment of bright light sources, mainly lasers, optical fibres replaced copper wires that were used for long-distance communication purposes before.

One might think that, because optical components superseded the electrical ones at long-distances, the replacement of integrated electrical circuits is soon to follow. But despite the superiority of photonic components concerning bandwidth for communication purposes, the optical technology has its drawbacks. Optical components use wave guiding features where similar microfabrication techniques are used as in the production of integrated circuits. Although the fabrication does not pose a restriction on the way to optical components with a high circuit density, it is the diffraction limit that does. The theory of diffraction shows that electromagnetic waves cannot be localised with higher precision than the wavelength of the light in the medium. Thus the miniaturisation of integrated optical components that are in use today, is bounded. Therefore other means of guiding light at sub-wavelength scale have to be found.

One possible solution are surface plasmon polaritons (SPP). Surface plasmon polaritons are collective oscillations of a metal's free electrons, that couple to the electromagnetic field in the medium outside the metal, like a dielectric. Because of this coupling, a light wave that excites surface plasmon polaritons becomes bound to the metal surface and can then be guided by it. With the hybrid nature of the surface plasmon polariton the light wave inherits the electron's sensitivity to the metal structure and can now be manipulated on scales much smaller than the free-space wavelength of the light itself. Hence surface plasmon polaritons are a mean of guiding light at a sub-wavelength scale.

The major drawback of surface plasmon polaritons is the strong attenuation of the wave that is guided. This is due to the fact, that metals show a strong absorption of electromagnetic radiation in the visible and infrared spectrum. Due to this damping, achievable propagation lengths with surface plasmon polaritons are of the order of only 10 µm, rendering them inadequate for transmission applications.

A way to circumvent the strong damping is the use of metal stripes of tens of nanometres thickness and a few micrometre width embedded in a dielectric. This way, not only a single metal-dielectric interface, but four are used, and the damping of metal is reduced significantly. Because the surface plasmon polariton does not exhibit damping in the dielectric around the metal but only in the metal itself, the drastic reduction of the portion of the electromagnetic field inside the metal by reducing the metal's cross-section leads to a tremendous increase in the surface plasmon polariton's propagation length. Furthermore, the oscillations at the four surfaces couple to form two well defined modes that span across the whole metal stripe. One of them exhibits propagation length in the millimetres range and is therefore called long-range surface plasmon polariton mode or syncopated long-range surface plasmon polariton (LRSPP). With a propagation length of several millimetres the long-range surface plasmon polariton is suitable for the application in photonic integrated circuits.

Wave guides based on the principle of long-range surface plasmon polaritons have

first been realised in 2000 by Charbonneau *et al.* [1]. Gold stripes of 8 µm width, 20 nm thickness and 3,5 mm length where clad in SiO_2 and excited with light of 1550 nm wavelength, soon other groups followed. For example Nikolajsen *et al.* [2] showed in 2002 that a LRSPP (or plasmonic) wave guide can be build with gold stripes in a polymer cladding, and, in 2008, Park *et al.* [3] succeeded in the construction of a plasmonic wave guide with a propagation loss lower than one dB/cm at a wavelength of 1,31 µm. But long-range surface plasmon polaritons can be used for more than just straight wave guides, also Y-splitters and directional couplers have been built (e.g. [4]). Even more sophisticated devices, for example a Mach-Zehnder interferometric modulator, a directional-coupler switch and an integrated power monitor have been realised [5]. All these devices have been built for telecom wavelengths (free-space wavelength: 1,31 µm – 1,55 µm), but also the visible and near-infrared spectrum are of interest. In the visible, LRSPP wave guides could be used, for example, to efficiently collect single photons from diamond nanocrystals. Another interesting application would be the demonstration of LRSPP-interference (Hong-Ou-Mandel effect) on the basis of a plasmonic beam splitter.

In this thesis the fabrication and test of a LRSPP wave guide for a free-space wavelength of 785 nm is presented. Starting with the necessary theory and numerical simulations to understand the phenomenon of long-range surface plasmon polaritons, the requirements for a wave guide are then derived and rendered into a design for a plasmonic wave guide. The fabrication process of the wave guide, mostly done in a clean room, is disclosed in detail in the next chapter. Subsequently, the experimental setup and the measurement scheme are described before the results are presented. The last chapter gives an outlook on possible applications and the further direction of the development of the LRSPP wave guide.

2. Theory of Long-Range Surface Plasmon Polaritons

In this chapter the theoretical background of long-range surface plasmon polaritons is presented. Starting with the model of electrons in a noble metal — the Drude-Sommerfeld-Theory — the basic properties of surface plasmon polaritons at a single metal-dielectric interface are derived and discussed, closely following [6] and [7]. Having understood the simplest case, the more complex situation of a thin metal film with two interfaces (dielectric-metal-dielectric) is discussed. If the metal film is thin enough, the surface plasmon polariton modes of the two surfaces couple to a mode spanning across the two interfaces. Finally, the modes of a thin metal stripe (i.e. a thin film of finite width) are examined with the help of numerical simulations [8]. Under the right circumstances the stripe exhibits a mode with low attenuation, called long-range surface plasmon polariton mode (LRSPP mode), that can be used to guide light waves.

2.1. The permittivity of metals

The picture of a free electron gas in a metal of the Drude-Sommerfeld-Theory will be used as a guide in order to create an intuitive understanding of the phenomenon of surface plasmon polaritons. With the help of this picture the effect of an applied electric field $\vec{E}$ on the free electrons of a metal is explained.

Mathematically the measure for the effect of an electric field on a medium and vice versa is the permittivity ε. It is usually expressed via the susceptibility $\chi_e(\omega)$

$$\varepsilon(\omega) = 1 + \chi_e(\omega). \tag{2.1}$$

The susceptibility relates the polarisation $\vec{P}(\omega)$ of a medium with the electric field inside a medium.

$$\vec{P}(\omega) = N \, e \, \vec{r}(\omega) = \varepsilon_0 \, \chi_e(\omega) \, \vec{E}(\omega), \tag{2.2}$$

where N, e and ε_0 represent the number of electrons per unit volume, the electron charge and the vacuum permittivity, respectively. $\vec{r}(\omega)$ stands for the displacement of an electron from its equilibrium position.

In the picture of the Drude-Sommerfeld-Theory the electrons are not bound to specific atoms, but are modelled as a free gas. Thus they do not experience a position dependent restoring force, only velocity dependent friction is present due to collisions. This leads to the equation of motion (compare e.g. [9])

$$m_e \frac{\partial^2 \vec{r}}{\partial t^2} + m_e \Gamma \frac{\partial \vec{r}}{\partial t} = e \, \vec{E}_0 \, e^{-i\omega t}, \tag{2.3}$$

with m_e the effective mass of a free electron and ω and $\vec{E}_0$ as the frequency and amplitude of the applied field. The damping factor Γ depends on the Fermi velocity v_F and the electron's mean free path length l as $\Gamma = \frac{v_F}{l}$.

It is now possible to derive the frequency dependent permittivity $\varepsilon_{free}(\omega)$ by substituting χ_e in equation (2.1) with (2.2) and using the solution for $\vec{r}$ of equation (2.3) that can be found with the ansatz $r(t) = r_0 \, e^{-i\omega t}$. Introducing the plasma frequency $\omega_p = \sqrt{Ne^2/m_e \, \varepsilon_0}$ the permittivity reads

$$\varepsilon_{free} = 1 - \frac{\omega_p^2}{\omega^2 + i\Gamma\omega}. \tag{2.4}$$

In a metal the plasma frequency ω_p describes the resonance frequency of the electron's oscillation around the metal ions. It is an important material parameter as it defines a boundary in the metal's response to electromagnetic radiation. For radiation with a frequency below the plasma frequency ($\omega < \omega_p$) the electrons follow the driving force of the applied electric field virtually instantly. Thus they oscillate with

the same frequency as the electric field and therefore reflect the incoming radiation almost totally. If the frequency of the applied electric field is increased above the plasma frequency ($\omega > \omega_p$), the optical properties of the metal change drastically. There the electron cannot longer follow the rapid oscillations of the electric field because of their mass. Therefore the electric field can pass through the metal without experiencing disturbances or losses due to charge oscillation and the metal becomes transparent.

Typically the plasma frequency of metals lies around $1,7 \cdot 10^{16}$ Hz or in terms of wavelength of an electromagnetic wave at 110 nm [10]. Therefore metals reflect light waves in the optical and infrared regime totally, since the electrons inside metals are able to follow the oscillation of the field. If the oscillation of the electrons becomes collective, then waves of varying charge densities are created, resulting in the phenomenon of surface plasmon polaritons. The charge density waves are referred to as plasmons, but strictly speaking a plasmon is the quasiparticle of the quantization of the (electron-)plasma oscillation.

The result for the permittivity ε_{free} in equation (2.4) is accurate for light in the infrared regime, but the picture of the Drude-Sommerfeld-Theory has to be extended in order to give precise results in the optical regime as well. In addition to the oscillations of the metal's free electrons, light in the optical regime is able to excite electrons of lower-lying bands into the conduction band. This effect has to be included in the derivation of the permittivity as well. It can be accounted for in much the same way the free electrons were treated. Because the electrons considered now are bound to atoms, their equation of motion has an additional term with a position dependent restoring force with spring constant α:

$$m\frac{\partial^2 \vec{r}}{\partial t^2} + m\gamma\frac{\partial \vec{r}}{\partial t} + \alpha\vec{r} = e\,\vec{E}_0\,e^{-i\omega t}, \tag{2.5}$$

with m being the effective mass of the bound electrons and γ the damping due to radiative losses. Solving the same way as in the free electron case, the permittivity due to bound electrons is

$$\varepsilon_{bound}(\omega) = 1 + \frac{\tilde{\omega}_p^2}{(\omega_0^2 - \omega^2) - i\gamma\omega}, \tag{2.6}$$

where $\tilde{\omega}_p = \sqrt{\tilde{N}e^2/m\,\varepsilon_0}$ and $\omega_0 = \sqrt{\alpha/m}$.

The sum of ε_{free} and ε_{bound} gives a good approximation of the permittivity ε of a metal under the illumination of light above a wavelength of 500 nm. For light with a wavelength smaller than 500 nm more than one interband transition would have to be considered. Already for the current case a constant offset of 6 has to be added to account for the integrated effect of all higher-energy interband transitions [6]. This yields for the full permittivity

$$\varepsilon(\omega) = 8 + \frac{\tilde{\omega}_p^2(\omega_0^2 - \omega^2)}{\omega^2\,(\gamma^2 - 2\omega_0^2) + \omega_0^4 + \omega^4} - \frac{\omega_p^2}{\Gamma^2 + \omega^2}$$
$$+ i\left(\frac{\gamma\omega\tilde{\omega}_p^2}{\gamma^2\omega^2 + (\omega_0^2 - \omega^2)^2} + \frac{\omega_p^2\Gamma}{\Gamma^2\omega + \omega^3}\right) \tag{2.7}$$

Using for example material constants for Gold [6], [11]

$$\omega_p = 13,8 \cdot 10^{15} \text{ s}^{-1} \qquad \tilde{\omega}_p = 45 \cdot 10^{14} \text{ s}^{-1} \qquad \omega_0 = 2\pi c/\tilde{\lambda}$$
$$\Gamma = 1,075 \cdot 10^{14} \text{ s}^{-1} \qquad \gamma = 9 \cdot 10^{14} \text{ s}^{-1} \qquad \tilde{\lambda} = 450 \text{ nm}$$

the permittivity for a wavelength of 785 nm can be calculated:

$$\varepsilon(\lambda = 785\text{nm}) = -23,3 + 1,8i \tag{2.8}$$
$$\varepsilon_{JC}(\lambda = 790\text{nm}) = -23,3 + 1,5i \tag{2.9}$$
$$\varepsilon_S(\lambda = 790\text{nm}) = -21,4 + 1,9i. \tag{2.10}$$

In order to demonstrate the validity of this approach the values ε_{JC} and ε_S are given in comparsion. These values were experimentally determined by Johnson and Christy [12] and Schröder [13], respectively. It is noteworthy that the real part of the permittivity is negative, leading to an imaginary part of the refractive index
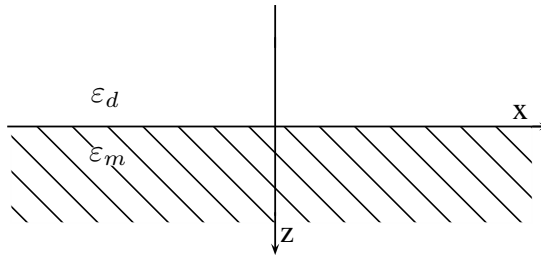
Figure 2.1.: Plane interface of a dielectric and a metallic conductor.

$n = \sqrt{\varepsilon\mu}$ (where μ is ~ 1, therefore set to 1). This large imaginary part causes strong damping of the electric field $\vec{E}$ inside the metal which is due to the dissipation of energy corresponding to the motion of electrons in the metal. The strong damping explains the small penetration depth of light into metals.

2.2. Surface plasmon polaritons on a single interface

In the next step towards surface plasmon polaritons, a single interface of a dielectric medium with permittivity $\varepsilon_d(\omega)$ and a metal $\varepsilon_m(\omega)$ is explored, revealing the basic properties of surface plasmon polaritons.

Let the interface between the two media lie in the plane $z = 0$ and let the medium in the half space $z > 0$ be the metal, thus $\varepsilon(\omega, z < 0) = \varepsilon_d(\omega)$ and $\varepsilon(\omega, z > 0) = \varepsilon_m(\omega)$ (see Fig. 2.1). For an arbitrary electric field vector $\vec{E}$ the only discontinuous component is the E_z component, since the interface is orthogonal to it. The other two components E_x and E_y are continuous across the interface as they are parallel to it. The conserved quantity in the z-direction is the displacement field D_z, thus $D_z = \varepsilon_0\varepsilon_d\, E_{d,z} = \varepsilon_0\varepsilon_m\, E_{m,z}$. The difference between ε_d and ε_m leads to the discontinuity in E_z, which in turn creates polarisation charges at the surface of the metal (Figure 2.2 a)). These surface charges are due to differences in the density of the metal's free electrons and can therefore be seen as plasmons. Because s-polarised waves have no E_z component, they cannot be responsible for surface plasmon polariton excitations. Hence, for the discussion only p-polarised waves are regarded [7].
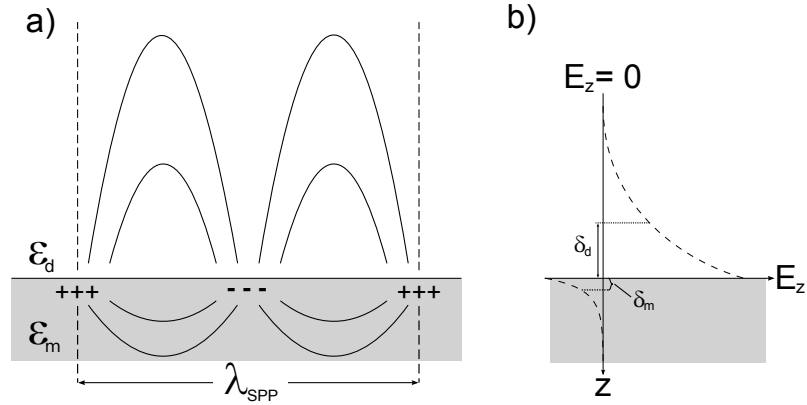
Figure 2.2.: Schematic sketch of the metal-dielectric interface. Both drawings illustrate that the majority of the electric field is located in the dielectric medium a) Electric field and charge distribution at the interface. b) z-component of the electric field in dependence of the distance to the interface.

The electric fields to be considered in the two halfspaces can be written as

$$\vec{E}_j = (E_{j,x}, 0, E_{j,z}) \; e^{i(k_x x - \omega t)} \; e^{ik_{j,z} z} \qquad j = \{d, m\}. \tag{2.11}$$

In order to find a dispersion relation, a system of four homogeneous equations is established. The continuity discussion above yields two equations — one for the component of $\vec{E}$ parallel to the surface and one for the perpendicular component of $\vec{D}$.

$$\vec{E}_{d,x} - \quad \vec{E}_{m,x} \; = 0 \qquad (\vec{E}_\parallel = \text{cont.}) \tag{2.12a}$$

$$\varepsilon_d \vec{E}_{d,z} - \varepsilon_m \vec{E}_{m,z} = 0 \qquad (\vec{D}_\perp = \text{cont.}). \tag{2.12b}$$

Because the half spaces are source free, $\nabla \cdot \vec{D}$ gives the two additional equations, yielding

$$k_x \vec{E}_{d,x} + k_{d,z} \vec{E}_{d,z} = 0 \qquad (\varepsilon_0 \varepsilon_d \, \nabla \cdot \vec{E_d}) \tag{2.13a}$$

$$k_x \vec{E}_{m,x} + k_{m,z} \vec{E}_{m,z} = 0 \qquad (\varepsilon_0 \varepsilon_m \, \nabla \cdot \vec{E_m}). \tag{2.13b}$$

Solutions for this set of equations can be found by setting the determinant to zero. One possible solution gives a relation between the permittivities and wavevectors of the two halfspaces:

$$\varepsilon_d k_{m,z} - \varepsilon_m k_{d,z} = 0. \tag{2.14}$$

For the second solution $k_x = 0$. As this does not describe a wave propagation along the x-axis, it is disregarded.

In order to attain a dispersion relation, the relation between the free space wavelength $k = \omega/c$ and the components of the wave vectors in the medium $(k_{j,x}, k_{j,z})$ is needed (keeping in mind that the y-component is zero),

$$k_x^2 + k_{j,z}^2 = \varepsilon_j k^2 \qquad j = \{d, m\}. \tag{2.15}$$

Using equation (2.14) and (2.15), dispersion relations for $k_x, k_{d,z}$ and $k_{m,z}$ can be established:

$$k_x^2 = \frac{\varepsilon_d \varepsilon_m}{\varepsilon_d + \varepsilon_m} k^2 \tag{2.16}$$

$$k_{d,z}^2 = \frac{\varepsilon_d^2}{\varepsilon_d + \varepsilon_m} k^2 \tag{2.17}$$

$$k_{m,z}^2 = \frac{\varepsilon_m^2}{\varepsilon_d + \varepsilon_m} k^2. \tag{2.18}$$

Those relations (2.16 – 2.18) give conditions for the existence of a surface plasmon polariton propagating in the x-direction, bound to the metal surface. Therefore k_x is expected to be real and on the other hand, the k_z components are expected to be imaginary. With imaginary k_y components the fields decay exponentially away from the interface, but are allowed to propagate along said surface. It is noteworthy that

k_x is not only the propagation constant for the electromagnetic field but also for the charge density waves that are excited by the electromagnetic field. This coupling between the electromagnetic field and the collective oscillations of the electrons at the metal's surface gives the phenomenon its name: surface plasmon polariton. The field and charge distribution along the metal-dielectric interface is depicted in figure 2.2.

As the dielectric function of a metal ε_m is complex (the imaginary part represents losses due to electron scattering), the wavenumber k_x becomes complex as well:

$$\varepsilon_m = \varepsilon'_m + i\ \varepsilon''_m, \qquad k_x = k'_x + i\ k''_x \qquad (\varepsilon'_m, \varepsilon''_m, k'_x, k''_x \in \Re) \qquad (2.19)$$

The real part of the wave number k'_x scales with $2\pi/\lambda_{SPP}$, whereas the imaginary part k''_x is a measure for the damping of the surface plasmon polariton in the direction of propagation (here the x-direction). Assuming that the dielectric has negligible loss ($\varepsilon_d \in \Re$) and with $|\varepsilon''_m| \ll |\varepsilon'_d|$ the dispersion relations (2.16 – 2.18) become

$$k'_x \approx \frac{\omega}{c} \sqrt{\frac{\varepsilon_d \varepsilon'_m}{\varepsilon_d + \varepsilon'_m}} \qquad (2.20)$$

$$k''_x \approx \frac{\omega}{c} \sqrt{\frac{\varepsilon_d \varepsilon'_m}{\varepsilon_d + \varepsilon'_m}} \frac{\varepsilon_d \varepsilon''_m}{2\varepsilon'_m (\varepsilon_d + \varepsilon'_m)} \qquad (2.21)$$

$$k_{m,z} \approx \frac{\omega}{c} \sqrt{\frac{\varepsilon'^2_m}{\varepsilon_d + \varepsilon'_m}} \left[1 + i\frac{\varepsilon''_m}{2\varepsilon'_m} \right] \qquad (2.22)$$

$$k_{d,z} \approx \frac{\omega}{c} \sqrt{\frac{\varepsilon^2_d}{\varepsilon_d + \varepsilon'_m}} \left[1 - i\frac{\varepsilon''_m}{2(\varepsilon_d + \varepsilon'_m)} \right], \qquad (2.23)$$

where $k_{m,z}$ and $k_{d,z}$ are determined to the first order in $|\varepsilon''_m|/|\varepsilon'_m|$ [6].

With these relations at hand, a few basic properties of surface plasmon polaritons can be calculated, for example with gold as the wave guide's metal. Its dielectric function is given by equation (2.9). For a permittivity of the dielectric medium of $\varepsilon_d(\lambda = 785\text{nm}) = 2,39$, which is the value of the dielectric medium that will be used in experiment, the surface plasmon polariton's wavelength is $\lambda_{\text{SPP}} = 481$ nm
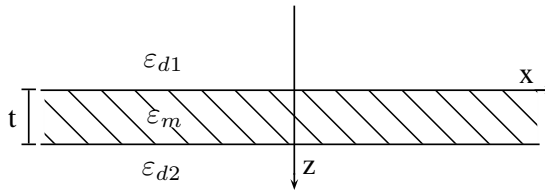
Figure 2.3.: Double interface of a dielectric-metal-dielectric sandwich structure

with an intensity propagation length $1/e$ $(1/2k_x'')$ of about 10 µm in the x-direction. The electric field in the z-direction, perpendicular to the surface, is evanescent and decays exponentially with increasing distance from the interface. Its decay length $\delta_j = 1/k_{j,z}$ differs for the two halfspaces as the field experiences different attenuations in the metal and in the dielectric. Figure 2.2 b) depicts this situation and the calculated decay lengths of the electric field for the two halfspaces are $\delta_m = 25$ nm for gold $(z > 0)$ and $\delta_d = 370$ nm for the dielectric $(z < 0)$.

The very short propagation length in the x-direction renders surface plasmon polaritons unsuitable for communication purposes, but a possible solution to increase the small propagation length can already been seen. The difference in penetration depth between the dielectric and the metal plays a very important role in the propagation of surface plasmon polaritons, because the majority of the propagating electric field is located in the dielectric where it is not subjected to absorption. Therefore by decreasing the fraction of the electric field inside the metal, the damping of the surface plasmon polariton can be reduced. The decay length into the gold also hints that parts of the electric field's evanescent tail could cross the metal barrier, if the thickness of the metal layer is chosen small enough. In this case the modes of the two interfaces can overlap and form new modes. This case was first predicted by Fukui in 1979 [14] and is discussed in the next section.

2.3. Surface plasmon polaritons on a double interface

The interaction of two surface plasmon polariton waves through a sufficiently small metal film was proposed by Fukui *et al.* [14]. In this case the two surface plasmon

polaritons of each interface couple, resulting in two mixed modes, called Fano modes [15],[16]. Because of the second interface three areas of different permittivity have to be considered. The metal film of thickness t (for its few occurrences the time variable is denoted T) stretches from $z = 0$ to $z = t$ and is surrounded by two dielectrics with permittivities ε_{d1} for $z < 0$ and ε_{d2} for $z > t$, see figure 2.3. Burke *et al.* [15] use the magnetic field to describe the surface plasmon polariton and then derive the electric field components E_x and E_z from Maxwell's equation via

$$E_{x,j} = \frac{i}{\omega \varepsilon_0 \varepsilon_j} \frac{\partial H_{y,j}}{\partial z}, \qquad E_{z,j} = -\frac{k_x}{\omega \varepsilon_0 \varepsilon_j} H_{y,j}, \qquad j = \{d1, d2, m\}. \tag{2.24}$$

Here it has already been taken into account that the magnetic field (equation (2.25)) has no y-dependence, eliminating all terms containing a derivative with respect to y. Furthermore, the derivative of $H_{y,j}$ with respect to x has already been calculated in the equation for $E_{z,j}$.

The magnetic field of a wave propagation in x-direction reads

$$\vec{H} = \hat{y} \; f(z) \; C \; e^{i(\omega T - k_x x)}, \tag{2.25}$$

with C a normalisation constant and $f(z)$ being the depth dependence of the magnetic field, chosen in a way that the tangential magnetic field is continuous at $z = 0$ and $z = t$

$$f(z) = \begin{cases} e^{S_{d1}z} & \text{if } z < 0, \\ \cosh(S_m z) + \frac{S_{d1}\varepsilon_m}{S_m \varepsilon_{d1}} \sinh(S_m z) & \text{if } 0 > z > t, \\ \left[\cosh(S_m t) + \frac{S_{d1}\varepsilon_m}{S_m \varepsilon_{d1}} \sinh(S_m t)\right] e^{-\frac{\varepsilon_m}{\varepsilon_{d2}} S_{d2}(z-t)} & \text{if } z > t \end{cases} \tag{2.26}$$

with

$$\begin{aligned} S_{d1}^2 &= k_x^2 - \varepsilon_{d1} k^2 \\ S_m^2 &= k_x^2 - \varepsilon_m k^2 \\ S_{d2}^2 &= k_x^2 - \varepsilon_{d2} k^2. \end{aligned} \tag{2.27}$$
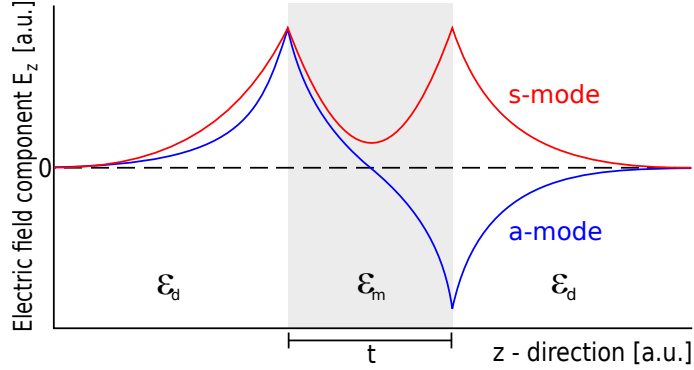
Figure 2.4.: Sketch of the amplitude of the E_z field component across a thin metal film. The surface plasmon polariton forms two modes, one with a symmetric (s-mode) and one with an asymmetric (a-mode) field distribution inside the metal film [15].

A dispersion relation can be established by demanding the continuity of the tangential electric field at $z = t$ [15]:

$$\tanh(S_m t)(\varepsilon_{d1}\varepsilon_{d2}S_m^2 + \varepsilon_m^2 S_{d1}S_{d2}) + \varepsilon_m S_m(\varepsilon_{d1}S_{d2} + \varepsilon_{d2}S_{d1}) = 0 \qquad (2.28)$$

For a thickness t of the metal much larger than the decay length of the electric field in the metal δ_m, $\tanh \to 1$ and equation (2.28) becomes

$$(S_{d1}\varepsilon_m + S_m\varepsilon_{d1})(S_{d2}\varepsilon_m + S_m\varepsilon_{d2}) = 0. \qquad (2.29)$$

In this case two solutions are found, each describing an independent interface — at $z = 0$ and $z = t$ — characterised by equations (2.20 – 2.23), Thus the two interfaces do not interact with one another. However, for the case of a metal film thinner than the penetration depth of the surface plasmon polariton, the two SPP modes couple and the dispersion relation (2.28) is not analytically solvable despite the very simple geometry of the structure. Therefore equation (2.28) has to be treated numerically. A full treatment of virtually all possible cases for the permittivities of the dielectric was done by Prade *et al.* [16] and yields for the case $\varepsilon_m > \varepsilon_{d1} > \varepsilon_{d2}$ and $\frac{1}{\varepsilon_m} < \frac{1}{\varepsilon_{d2}} - \frac{1}{\varepsilon_{d1}}$ the predicted Fano modes.
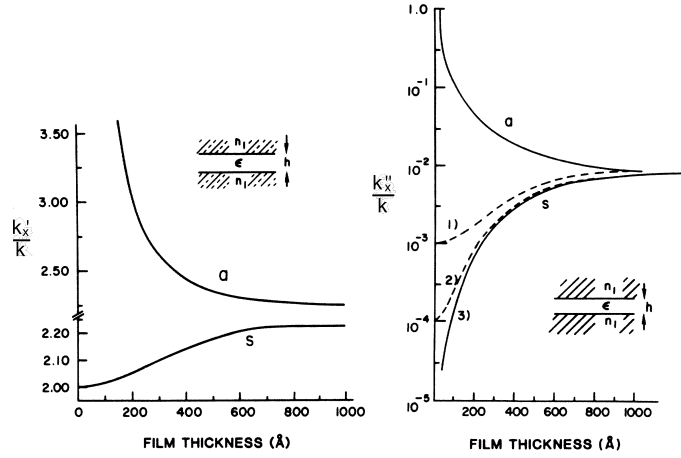
Figure 2.5.: Normalized complex propagation wave vector k_y/k as a function of the film thickness for the symmetric structure with $\sqrt{\varepsilon_1} = 2.0$. a and s refer to the asymmetric and symmetric mode, respectively. (1) $\sqrt{\varepsilon_1} = 2.0 - 0.001\,i$, (2) $\sqrt{\varepsilon_1} = 2.0 - 0.0001\,i$, and (3) $\sqrt{\varepsilon_1} = 2.0$, $\varepsilon_m = -19 - 0.53\,i$. Adapted from [15].

In the special case of a symmetric dielectric cladding — $\varepsilon_{d1} = \varepsilon_{d2} = \varepsilon_d$ and $\varepsilon_d < \varepsilon_m$ — two SPP modes are identified. One with a symmetric electric field distribution inside the metal (called s-mode) and the other one with an asymmetric field distribution (called a-mode), see figure 2.4. A very interesting feature of the s-mode is the fact that it becomes lossless as the metal film thickness t converges to zero (as long as the dielectric function of the dielectric has no imaginary part) [15]. Figure 2.5 shows a solution of the dispersion relation (2.28) at a wavelength of 633 nm, where the real and imaginary part of k_x (called β_R and β_I respectively) are normalised with the free space wavenumber $k = \omega/c$ and plotted against the film thickness t. The drop in the damping of the s-mode can clearly be seen for $t \to 0$. The low dissipation of the s-mode increases the propagation length of the surface plasmon polariton tremendously. For a silver film of 15 nm thickness and a cladding with $\sqrt{\varepsilon_d} = 1,5$ at 633 nm the propagation length is around 610 µm, which is 40 times longer than that of a surface plasmon polariton on a single interface [15].

In summary, the introduction of a second interface within the penetration depth
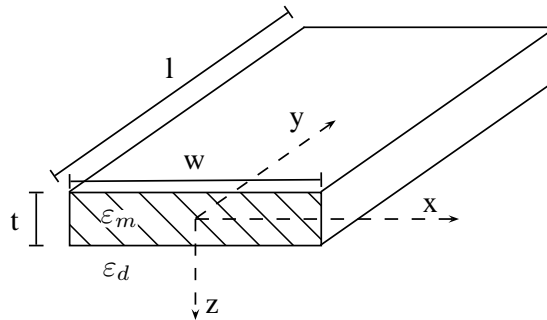
Figure 2.6.: Schematic of a metal stripe surrounded by a dielectric used for long-range surface plasmon polariton propagation. Propagation direction is the y-direction.

of the surface plasmon polariton into the metal leads to a drastic increase of the propagation length of the surface plasmon polariton. In the next chapter it is shown that an ever bigger increase in the surface plasmon polariton's propagation length can be achieved if metal stripes with a finite width instead of an infinite metal film are used.

2.4. Long-range surface plasmon polaritons in metal stripes

In the structures discussed so far, confinement of the SPP modes has been achieved only in one dimension. Two-dimensional confinement can be realised by embedding a thin metal stripe of width w in a dielectric, as shown in figure 2.6. Vast numerical analysis of the electric fields in such structures has been done by Berini in 1999 [8]. Silver stripes in a dielectric cladding are modelled for a stripe width w between 1 and $0,25$ µm, a metal thickness t between 5 and 200 nm, a permittivity of the dielectric cladding ε_d between 1 and 4 and the free-space wavelength is varied from 0,5 to 2 µm. The permittivity of silver used is $\varepsilon_m = -19 - 0,53i$ and unless otherwise stated a free-space wavelength of 633 nm and a permittivity of the dielectric medium of $\varepsilon_d = 4$ are assumed. Note that the direction of propagation of the surface plasmon polaritons is now the y-direction.

The first thing to note about the stripe wave guide is that it, just like the slab wave guide, supports several modes. But in contrast to the slab wave guide that exhibited two modes (Fig. 2.5) with different field distributions inside the metal, the stripe wave guide shows four fundamental modes, called ss_b^0, as_b^0, sa_b^0 and aa_b^0 (Fig. 2.7). The field distributions are symmetric or asymmetric with respect to the two axes of the stripe's cross-section, giving four possible field symmetries. Moreover each of the fundamental modes can support higher order modes with several extrema in the distribution of the real part of the electric field in z-direction $\mathrm{Re}(E_z)$. The connotation of the modes follows these rules: The pair of letters, each of them either s or a, indicate the field symmetry with respect to the z- and x-axes, respectively, where 's' stands for a symmetric field distribution and 'a' for an asymmetric one. The subscript b indicates that the SPP mode is bound (leaky and growing SPP modes are also possible, see e.g. [15]) and the number in the superscript counts the number of extrema of E_z along the x-axis, thus the higher order modes, where 0 refers to the fundamental mode).

2.4.1. Characteristics of the long-range surface plasmon polariton mode

In order for a long ranging surface plasmon polariton mode (LRSPP mode) to exist, the metal stripes' geometry has to fulfil the condition $w/t \gg 1$ and the only mode of interest due to its small attenuation is the fundamental mode that is symmetric with respect to both axes, ss_b^0. For metal thicknesses $t < 40$ nm the ss_b^0 or LRSPP mode experiences a drop of the attenuation whose magnitude is similar to the one of the s-mode of the symmetric slab wave guide described above (section 2.3), thus allowing a long range propagation of the ss_b^0 mode . All other modes show either an increase in damping with thinner metal layers (aa_b^0, sa_b^0, sa_b^1) or experience a cut-off thickness and are not supported for thickness below the cut-off (as_b^0, ss_b^1). This can be seen from figure 2.7, that shows the normalised attenuation constant k_y''/k over the metal thickness t.
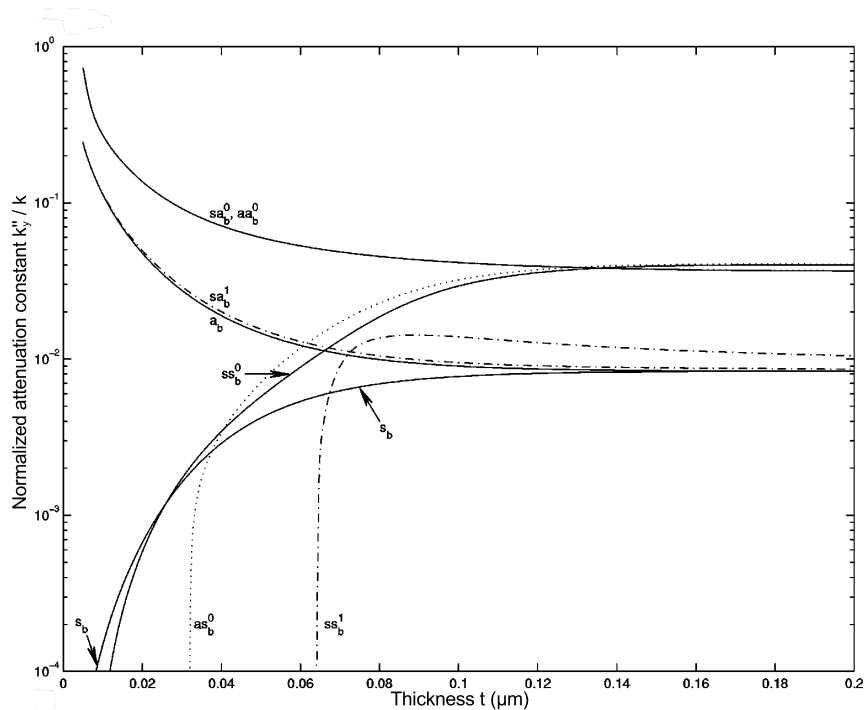
Figure 2.7.: Normalised attenuation constant versus metal thickness t with stripe
width $w = 0,5$ µm. In addition to the four fundamental modes in the
gold stripe, the first higher order modes sa_b^1 and ss_b^1 are shown, as well
as the s- and a-mode of the infinite metal film (denoted s_b and a_b here).
Adapted from [8].

The main transverse electric field for all metal stripes with a geometry of $w/t \gg 1$
is the one in the z-direction, E_z. On the example of the LRSPP mode, Berini
showed that the magnitude of the two other electric field components decrease with
decreasing metal thickness, leaving the E_z field as the dominant contribution to the
total electric field $\vec{E}$. With the two field components vanishing for decreasing metal
thicknesses, the LRSPP mode evolves into a TEM mode where only the E_z and H_x
fields are present [8].

Another important feature of the LRSPP mode is that the field distribution obtains
a Gaussian-like shape as the stripe thickness t decreases. For thick metal films the
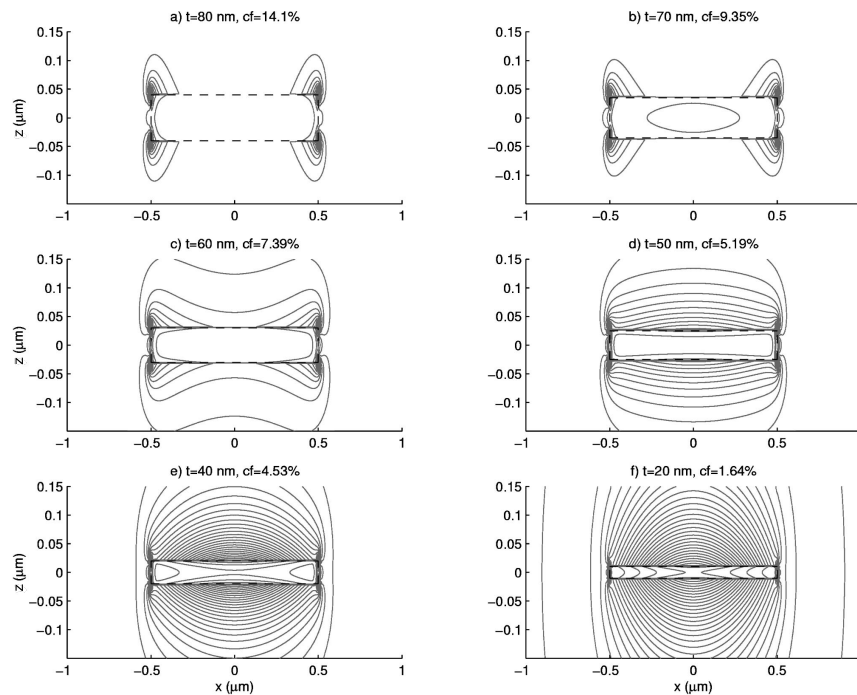
Figure 2.8.: Contour plot of the real part of the Poynting vector S_y associated with the ss_b^0 mode for metal films of width $w = 1$ µm and various thicknesses. The outline of the stripe's cross-section is shown as the rectangular dashed contour. Adapted from [8].

field is localised at the sides of the metal stripe and expands towards the middle with decreasing metal thickness until the field distribution is almost Gaussian. This evolution can be seen in figure 2.8, where a contour plot of the Poynting vector $S_y = \frac{1}{2}(E_x H_z^* - E_z H_x^*)$ in propagation direction for various thickness can be seen. Especially the E_z component obtains a Gaussian-like shape along the wave guide width, which allows the excitation of the ss_b^0 mode via end-fire coupling [17]. This coupling scheme is commonly used in integrated optics and will be explained in section 5.1. In principle, the mode profile of the excitation beam is matched with the mode profile of the gold stripe in order maximise the overlap between the two modes.

Berini [8] also examined the strong influence of the permittivity of the dielectric cladding on the attenuation of the LRSPP mode. It can be seen in Fig. 2.9 that
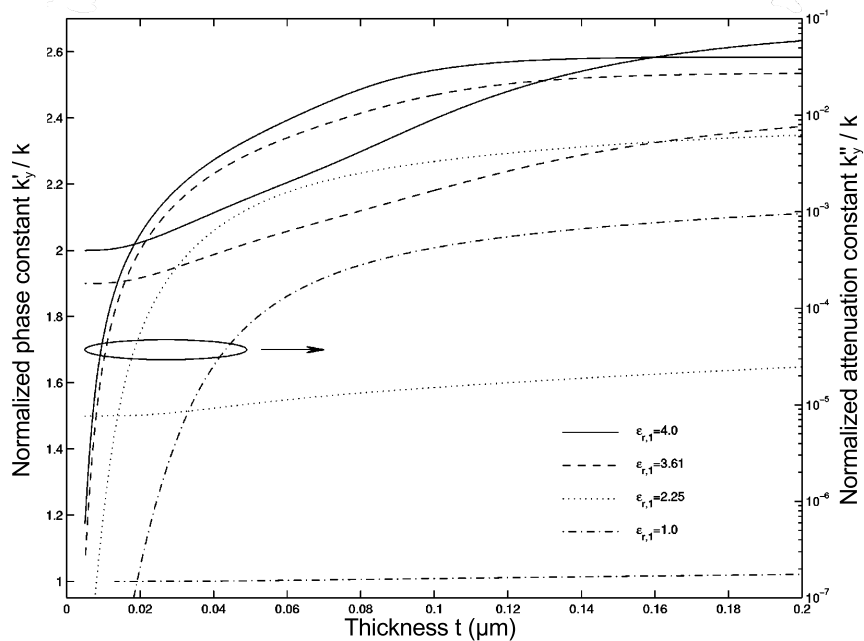
Figure 2.9.: Normalised propagation k'_y/k and normalised attenuation constant k''_y/k as a function of the metal thickness t ($w = 0.5$ µm) for various permittivities of the metal surrounding dielectric ε_d (in the plot $\varepsilon_{r,1}$). The normalized phase constant is plotted on the left axis and the normalized attenuation constant is plotted on the right one. Adapted from [8].

the normalised attenuation is reduced by almost four orders of magnitude as the cladding permittivity is lowered from $\varepsilon_d = 4$ to $\varepsilon_d = 1$ [8].

So far all simulations have been performed at a wavelength of 633 nm. In the last part of [8] the frequency dependence of the attenuation is modelled. As a result, a decrease of the attenuation with an increase in wavelength can be recognized. A plot of the mode power attenuation MPA can be seen in Fig. 2.10, showing a difference in attenuation of roughly two orders of magnitude between a free-space wavelength of 785 nm and 1550 nm. In detail, the mode power attenuation in terms of dB/mm is given by

$$MPA = k_y'' \frac{20}{1000} \log(e). \tag{2.30}$$
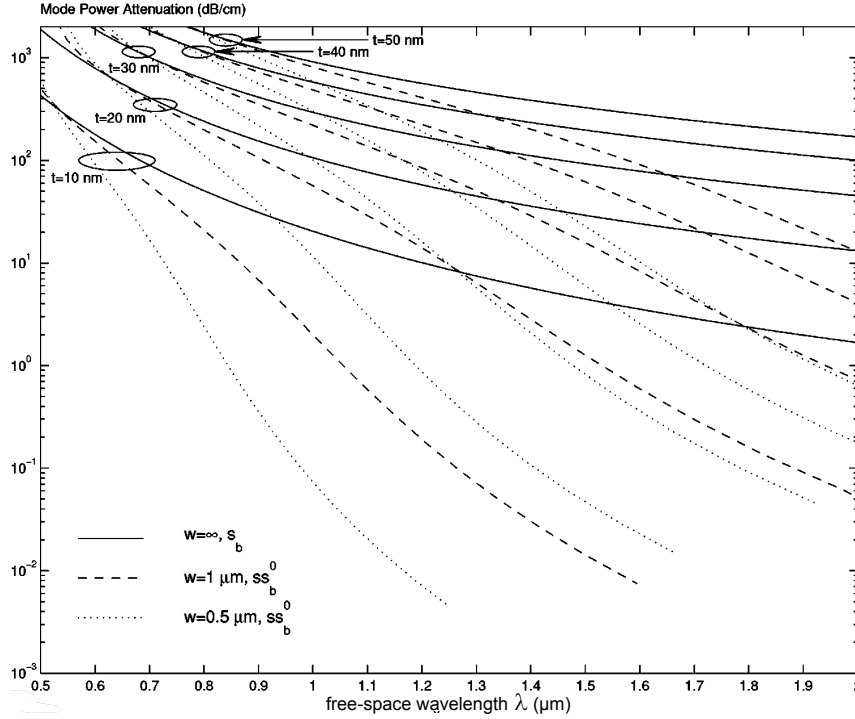
Figure 2.10.: Calculated Mode Power Attenuation in dB/cm of the ss_b^0 mode in dependence of the free space wavelength of the incident light. Metal stripe width $w = 0.5$ µm and $w = 1$ µm and various thicknesses t. The s-mode supported for the case $w = \infty$ is shown for comparison (solid lines). Adapted from [8].

With the model of Berini [8] at hand the vast increase in propagation length compared with the single interface can be demonstrated. Again assuming a free-space wavelength of 785 nm and a wave guide geometry of $w = 1$ µm, $t = 15$ nm and cladding permittivity of $\varepsilon_d = 2,25$, the deduced intensity propagation length $1/e$ $(1/2k_y'')$ is roughly 4,5 mm (corresponding to a damping of 1 dB/mm). This is an increase in the propagation length compared to the single interface in section 2.2

of two orders of magnitude and shows that long-range surface plasmon polaritons are ideally suited for applications that require propagation over distances of several mm.

3. Wave guide design

The design of the wave guide, especially the decision for the materials involved, is a harder task than the theory might reveal at first. In theory a wave guide on the basis of long-range surface plasmon polaritons consists of a metal stripe with rectangular cross section in a dielectric cladding where the stripe has a thickness of tens of nanometers and a width of a few micrometers. The attenuation of the long-range surface plasmon polariton decreases with decreasing stripe thickness and width and a lower permittivity of the dielectric cladding reduces the attenuation as well. The metal is preferably picked such that its permittivity has a large but negative real part and small imaginary part. Practically, these theoretical requirements pose difficulties. Especially the assumption of a dielectric cladding with a single permittivity ε_d is difficult to achieve in reality, but deviations of a single value of ε_d can have strong influences on the attenuation of the long-range surface plasmon polariton.

3.1. Asymmetry in the permittivity of the cladding

The theoretical computations performed in section 2.4 assume symmetry in the permittivity of the cladding, i.e $\varepsilon_{d1} = \varepsilon_{d2}$, but during the fabrication process small differences Δ in this symmetry can occur, for example

$$n_1 = n_2 + \Delta \tag{3.1}$$

$$\varepsilon_{d1} = n_1^2 = (n_2 + \Delta)^2 = \varepsilon_{d2}. \tag{3.2}$$

The influence of this asymmetry in the refractive index on the attenuation of the long-range surface plasmon polariton has been analysed in detail by Breukelaar and Berini [18] for the slab and by Berini [19] for the stripe wave guide. The LRSPP
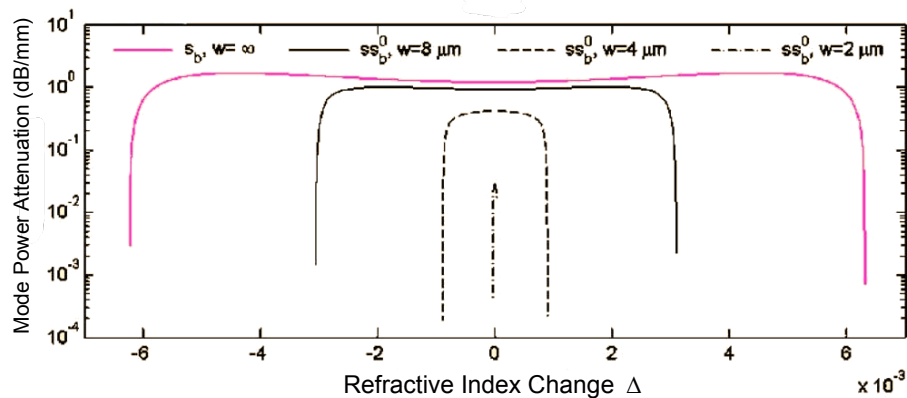
25

Figure 3.1.: Mode power attenuation as a function of the refractive index asymmetry Δ for various stripe widths with thickness $t = 20$ nm. $\varepsilon_{d1} = 1{,}447$. Adapted from [19].

mode ss_b^0 exhibits a cut-off if the asymmetry exceeds a certain value, for example $\Delta = 1 \cdot 10^{-3}$ for a stripe of 4 µm width. Figure 3.1 illustrates the cut-off asymmetry for gold stripes at a free-space wavelength of 1550 nm. The allowed cut-off asymmetry gets smaller with decreasing stripe dimensions (for the thickness dependence see [18]) reaching $5 \cdot 10^{-5}$ for a 2 µm wide stripe. With increasing asymmetry, but before cut-off, the fields expand into the medium with the higher refractive index, strongly deforming the mode. At the same time the mode's attenuation falls until the cut-off is reached, because the portion of the field in the dielectric rises. Schemes to use this effect and operate near cut-off face practical difficulties. As the mode expands into one of the media, it deforms and looses its Gaussian-like shape, thus becoming more difficult to excite via end-fire coupling (see section 5.1). Therefore a use of this effect would be accompanied by a drastic increase in coupling loss [19]. In summary, an asymmetry in the refractive index between the upper and the lower cladding reinforces the coupling loss and quickly leads to a mode cut-off. Therefore the asymmetry has to be kept as low as possible.

There are several ways of matching the refractive indices of the claddings (i.e. the portion of the dielectric medium above and below the metal) as they are applied in different fabrication steps. In a dynamic set-up the lower cladding and the upper

Substrate (Schott N-PSK3)	n = 1,546
Polymer (BCB)	n = 1,545
Gold	
Substrate (Schott N-PSK3)	n = 1,546

Figure 3.2.: Design for the plasmonic wave guide. The gold stripes are cladded in a layer of BCB, which is sandwiched between two substrates.

cladding consist of two different materials with roughly the same refractive index, but their temperature dependence of the refractive index differs strongly. Thus the indices can be matched by controlling the temperature of the wave guide [19].

Alternatively, in a static approach the indices are matched during the fabrication [2]. Usually the same material is used for the upper and lower cladding, but the material has to be picked carefully. It has to be assured that the material does not change its refractive index throughout the fabrication process. The wave guide in this experiment comprises of gold stripes in a polymer cladding, following the static approach of Nikolajsen [2].

3.2. Gold as the wave guide metal

The results presented in section 2.4 are based on silver as the wave guide metal, but silver has a practical disadvantage: it oxidates in air. Thus the purity of the silver stripes cannot be guaranteed, as the silver would be exposed to air during the fabrication process. Gold, on the other hand, is inert during the fabrication process and is therefore a good alternative.

In [19] Berini compares silver with gold wave guides theoretically to find, that the confinement is roughly equal but gold exhibits stronger damping than silver. He suggests that the damping of gold is increased by a factor of 3,7 at a free-space wavelength of 1,5 µm, but could verify this prediction only qualitatively. Thus the

use of gold in the wave guide will lead to a stronger attenuation than silver, but does not affect the LRSPP mode in any other way, rendering it the best choice as the wave guide metal.

3.3. Outline of the wave guide

The design of the wave guide used in the experiment follows the one used by Nikolajsen *et al.* [2] and a cross-section of the designed wave guide can be seen in figure 3.2. The gold stripes are clad in benzocyclobutene (BCB), a polymer sold by The Dow Chemical Company under the trade name of Cyclotene. The BCB comes as an unpolymerised, highly viscous liquid that is applied on the base substrate via spin coating. The polymerisation is done in a convection oven where temperature and duration determine the degree of polymerisation. The used substrates are 15x15 mm Schott N-PSK3 glass blanks and the BCB is applied as a 15 µm layer. Onto that, the gold stripes are deposited via photolithography and electron beam evaporation and coated with a second, 35 µm thick layer of BCB. This layer it then sealed with another N-PSK3 substrate. The photo mask used in the lithography is designed to give gold stripes of 0,5; 1,0; 1,5; 2; 4; and 6 µm width and a length of 7 mm. For each width 10 stripes (6 for the 6 µm width) are formed and grouped together with a separation of 30 µm and 600 µm between neighbouring stripes and groups, respectively. The design of the photomask is illustrated schematically in figure 3.3, showing the groups of gold stripes of different width. The rectangular patterns between the groups are introduced for reasons of orientation, because the gold stripes, even as groups, are barely visible with the naked eye. The gold thickness is chosen to be 15 nm as it marks the lower limit where gold can safely be evaporated as a homogeneous layer, thinner gold layers would suffer from inhomogeneities like islandisation.

Boltasseva *et al.* performed attenuation measurements on wave guides of this design with a free-space wavelength of 1550 nm [4]. For a gold stripe of 8 µm width and 15 nm thickness a attenuation of 5-8 dB/cm was found. The coupling loss with end-fire
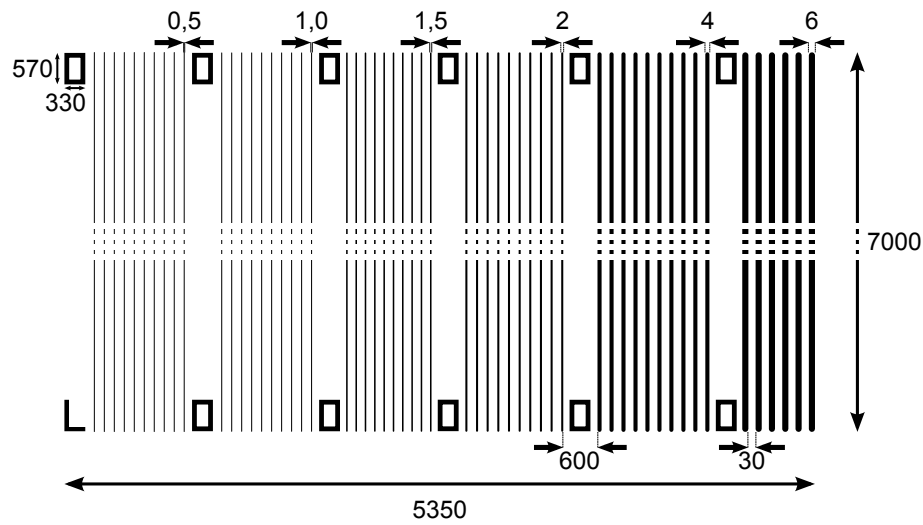
Figure 3.3.: Schematic sketch of the photomask and with that the gold pattern of the wave guide

Coupling (i.e. the loss that occurs on the facets of the wave guide during coupling) was also quantified to 0,5 dB per facet and 1,5 dB per facet for 10 µm and 4 µm wide gold ($t = 15$ nm) stripes, respectively. The mode field diameter of the LRSPP mode has been measured as well and found to be ~10 µm for 15 nm thick gold stripe of width between 3 and 12 µm [4].

Even though in [8] and especially in figure 2.10 the mode power attenuation for a free-space wavelength of 785 nm is predicted to be orders of magnitude higher than for incident light of 1550 nm wavelength, the results of Boltasseva give rise to the assumption that long-range surface plasmon polariton propagation at a free-space wavelength of 785 nm is possible as well.

In summary, the wave guide to be built consists of 56 gold stripes cladded by two BCB layer of 15 µm and 35 µm thickness in between two Schott N-PSK3 glass substrates. The gold stripes have a thickness of $t = 15$ nm and a width w between 0,5 µm and 6 µm. The length l of the wave guide varies between 1 mm and 5 mm. The expected damping cannot be predicted reliably, but is assumed to be one order of magnitude larger than the one by Boltasseva [4].

4. Wave guide fabrication

In the previous chapter the design of the wave guide was developed, while keeping the limitations of the microfabrication process in mind. Therefore gold as the wave guide metal is used, as well as the polymer BCB (Cyclotene), whose refractive index is easily reproducible.

The manufacturing process of the wave guide relies on photolithography and electron beam fabrication as the fabrication techniques. The concept of the two techniques shall be explained before the actual fabrication process of the wave guide is presented.

4.1. Underlying principle of photolithography

Photolithography is a microfabrication technique that engraves the geometries of the desired metal structures from a master photomask (see figure 3.3) into a layer of photoresist that has been applied on the substrate. The process steps are illustrated in figure 4.1 [20]. In a first step a photosensitive resin is applied to a substrate that shall carry the metal structures (figure 4.1, 1. & 2.). Subsequently the photomask is placed directly on the substrate with the photoresist and is then illuminated with ultraviolet light (figure 4.1, 3.). As the photoresist is sensitive to ultraviolet light it changes its chemical properties in the regions exposed to the light, in a way that the exposed regions are rendered soluble in basic solution. The substrate with the exposed photoresist is immersed in a basic solution, called developer, until the photoresist has disintegrated in the exposed areas (figure 4.1, 4.). One is left with a coated substrate except for the regions defined by the photomask.

1. Coat and prebake LOR

4. Develop resist and LOR. LOR develops isotropically, creating a bi-layer reentrant sidewall profile

2. Coat and prebake imaging resist

5. Deposit film. The reentrant profile ensures discontinuous film deposition.

3. Expose imaging resist

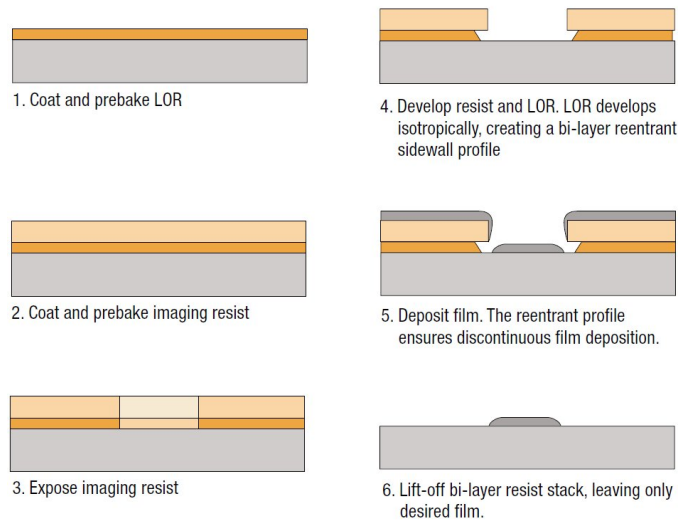6. Lift-off bi-layer resist stack, leaving only desired film.

Figure 4.1.: Process steps for photolithography with a sacrificial layer (LOR) in order to create an undercut [20].

The deposition of the gold is done with electron beam evaporation. In a ultra-high vacuum an electron beam is focussed into a pot of gold. The generated gold vapour precipitates on all surfaces in the evaporation chamber, including the substrate and the photoresist (figure 4.1, 5.).

In the final step, the lift-off, the substrate is immersed in a solvent to remove the photoresist. Because the photoresist covered up the areas that shall be blank, the gold structures on the substrate will have the geometry of the photomask (figure 4.1, 6.).

Besides the photoresist, an additional layer below the photoresist is shown in figure 4.1 as well. This layer is a so called sacrificial layer or lift-off resist (LOR) and is used to create an undercut in the resist structure. It is not photosensitive but it dissolves in the developer, and is stripped of in the solvent together with the photoresist. The undercut improves the separation between the photoresist and the substrate, creating a distinct layer of gold on the substrate. This reduces the forces on the gold during the lift-off process, making the deposition of gold on top of BCB

possible in the first place, because no adhesion promoters for the gold can be used (see appendix A.1 for more details).

4.2. Manufacturing process

The manufacturing process has been done mainly in the clean room of the chair for solid states physics of Prof. Dr. Kotthaus, part of the nanophysics group of the Ludwig-Maximilians-Universität, München.

The fabrication included the following steps:

1. Substrate cleaning
2. Application and soft cure of the lower cladding
3. Lithography
4. Electron beam evaporation
5. Lift-Off
6. Application of the upper cladding and the top substrate
7. Hard cure of the entire die
8. Sawing the die into individual wave guides
9. Polishing the wave guide

The table 4.1 gives an overview of the process parameters involved in the production process. Each of the parameters influences the outcome of the fabrication in a certain way and had to be adjusted carefully. An example of the adjustment process is given in the appendix A.1.2 on the basis of the creation of an undercut.

Substrate cleaning

The used substrates are made out of Schott N-PSK3 glass and have the dimensions of 15x15x1 mm. The substrates are cleaned prior to use. This is done in acetone in an ultrasonic bath. In order to remove all organic residues, the substrates subsequently undergo an oxygen plasma treatment. In a vacuum an oxygen plasma is ignited that reacts with any organic residue on the substrate, separating it from the surface.

1	**Cleaning**			
2	**Lower Cladding**			
	Adhesion promoter			
	Resist spinning	300 rpm, 5 s	2500 rpm, 15 s	
	BCB			
	Resist spinning	600 rpm, 6 s	1000 rpm, 30 s	10000 rpm, 1,5 s
	Soft Bake	100℃, 60 s		
	Soft Cure	209℃, 40 min		
3	**Lithography**			
	Lift-off resist			
	Resist spinning	800 rpm, 3 s	4000 rpm, 30 s	
	Soft Bake	180℃, 180 s		
	Photoresist			
	Resist spinning	800 rpm, 3 s	5000 rpm, 30 s	
	Soft Bake	115℃, 90 s		
	Exposure	40 s		
	Developement	2 min		
	Ratio Dev:H_2O	1:3		
4	**e-Beam evap.**	rate	thickness	
	Gold	1 Å/s	15,1 nm	
5	**Lift-off**	60 ℃, 90 min	in NMP	
6	**Upper cladding**	BCB		
	Resist spinning	600 rpm, 20 s		
	Soft Bake	100℃, 60 s		
7	**Hard Cure**	233℃, 120 min		
8	**Sawing**			
	Balance weight	90 g		
9	**Polish**			
	Grain size [μm]	5, 3, 1 and 0,3		

Table 4.1.: Overview of all process parameters for the fabrication of a wave guide
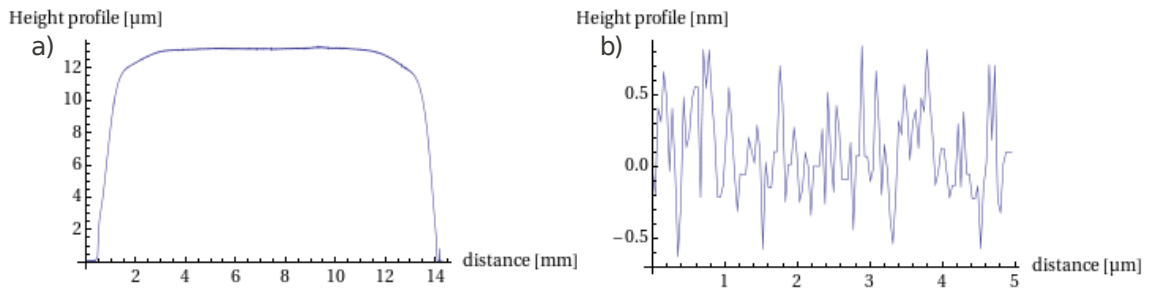
Figure 4.2.: Profiles of the lower layer of BCB with removed edge bead and after soft cure, a) Profile over the entire substrate b) Roughness of the surface, taken with an AFM

The lower cladding

The cleaned substrate is coated with the BCB (Cyclotene 3022-57, The Dow Chemical Company). For better adhesion on the substrate the Dow Adhesion Promoter AP3000 is applied first, followed by the Cyclotene to form a 13 µm BCB layer. All of the used resins are applied with the spin-coating technique. A few drops of the liquid resin are placed on the substrate which is then rapidly rotated with a few thousands rounds per minute so that the resin spreads homogeneously over the substrate, where faster rotation creates thinner layers. The edge bead of the BCB — a ridge of excessive resin at the edge of the substrate — has to be removed in order to assure a flat surface for lithography. Otherwise the edge bead would interfere with the spreading of the resists applied in the next step, creating uncontrolled resist thicknesses. The edge bead removal is done manually with a razor blade. A perimeter of about 1 mm around the edge of the substrate is cleared by scratching off the BCB with the blade. Subsequently the sample is shortly baked on a hotplate (60 s, 105℃) to minimize flowing, before it is soft cured in an oven for 40 minutes at 210℃ . The degree of polymerisation after the soft cure is approximately 80% [21], assuring mechanical stability throughout the lithographic process. At the same time it allows the bonding with the upper BCB layer into one monolithic layer during the final hard cure. In order to prevent oxidation of the BCB, which would lead to inhomogeneities in the refractive index, the oven is flooded with nitrogen during the cure. Figure 4.2 shows the profile and surface roughness of the finished BCB layer.
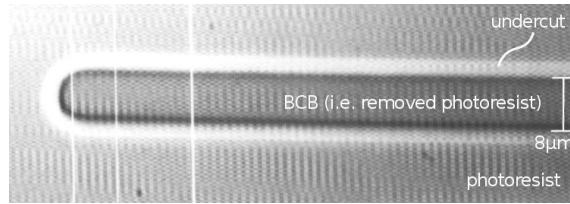
35

Figure 4.3.: Microscope picture of the photoresist and lift-off resist after development. The undercut shows as a bright margin around the stripe. (designed stripe width: 6µm

Lithography

The lithography is done on top of the soft cured BCB layer. As the sacrificial layer the lift-off resist LOR 3B from MicroChem Corp is applied with spin-coating to form a layer of 300 nm thickness [20] and baked on a hotplate at 180℃ for 180 s. The temperature and time of the lift-off resist's bake define the dissolution rate in the developer. The hotter or longer the bake, the smaller the etch rate and thus the growth of the undercut. The photoresist S1813 G2 from Rohm and Haas is applied on top of the lift-off resist via spin-coating to a layer of approximately 1,2 µm thickness [22] and baked at 115℃ for 90 s. Similar to the lift-off resist, the bake of the photoresist influences its dissolution rate in the developer. The substrate is then exposed to ultraviolet light through the photomask mentioned in section 3.3 for 40 s and developed in Rohm and Haas' Microposit 351 Developer for 120 s. The make-up of the development bath is 3 parts by volume deionized water on 1 part by volume developer.

A successful undercut created by the lithography can already be seen in an optical microscope (figure 4.3) as a white perimeter around the structures. For a thorough assessment of the undercut an examination in a scanning electron microscope is necessary, where the height and depth of the undercut can be evaluated. Figure 4.4 shows a scanning electron picture of an undercut created with a shorter development time of 80 s. The undercut can be seen clearly and it has the expected height, whereas the photoresist's edges are not optimal but acceptable.
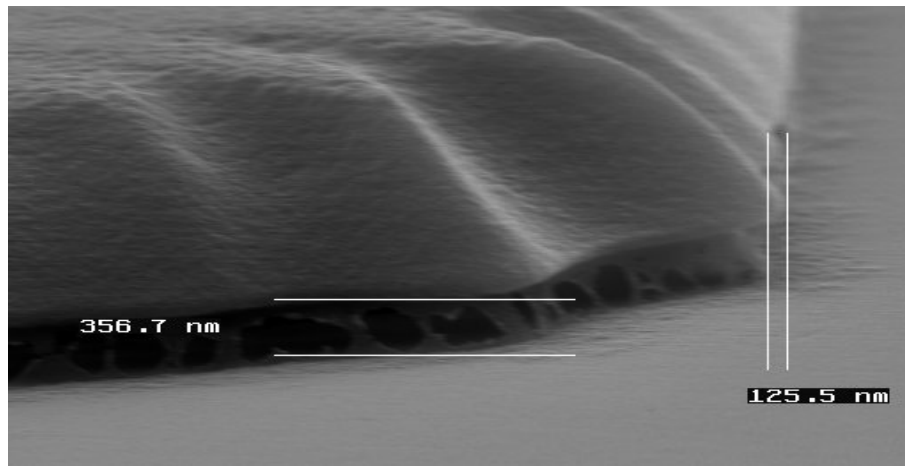
Figure 4.4.: Picture of an undercut taken with a scanning electron microscope at a magnification of 19500x.

Electron beam evaporation

The deposition of the gold is done with electron beam evaporation. The substrate is inserted into the vacuum of the evaporation chamber before the high voltage for the electron beam is activated. The beam voltage and current are picked in a way that a constant deposition rate of 1 Å/s is achieved. A shutter, which shields the substrate, is opened by the time the constant evaporation rate is attained and closed as soon as the desired thickness of the gold layer is reached. Typically the deposition rate and thickness are measured with an oscillating crystal and the pressure in the evaporation chamber is usually between $1 \cdot 10^{-7} - 6 \cdot 10^{-7}$ mbar.

Lift-off

After the deposition of the gold layer the photo- and the lift-off resist have to be removed. This is done in a bath of N-Methyl-2-pyrrolidone (NMP), a solvent with low volatility and low flammability. The dies (substrates with deposited gold structure) are submerged in the solvent upside-down, where a watch glass is used in order to prevent the gold from scratching, but simultaneously, allowing the solved resists
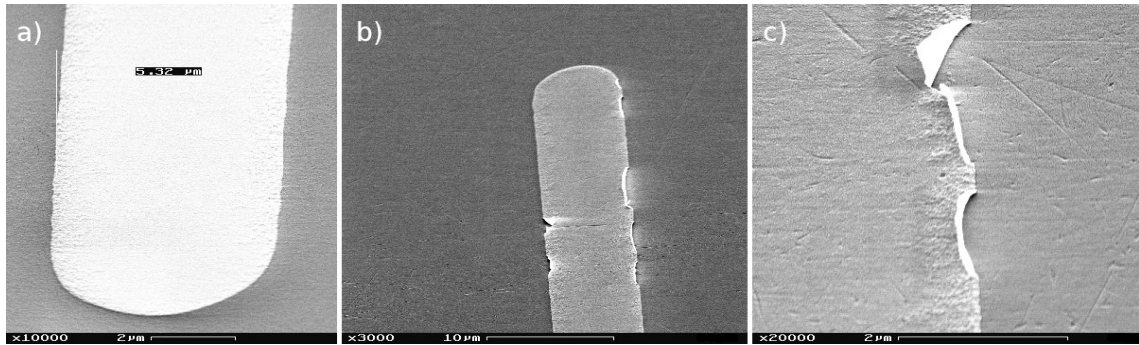
Figure 4.5.: Scanning electron microscope picture of gold stripes after the lift-off. (a) stripe with good edge quality (b),(c) stripes with lower edge quality. The gold layer lifted at the edges due to poor lift-off.

with the residual gold, to fall to the ground. Mechanical action such as shaking or an ultrasonic bath are counterproductive. Even though they speed up the lift-off process, they lead to uneven and elevated edges. The duration of the dwell in the NMP bath is at least 90 minutes at 60℃ . After that the dies are rinsed with acetone, then IPA and blown dry with nitrogen.

The quality and width of the gold stripes can be determined after the lift-off. The scanning electron microscope is suitable for a good overview of the stripes' shape and the defects. The atomic force microscope (AFM) is used for a precise width and height measurement of the stripe. For both techniques the die has to be sputtered with gold, rendering it useless for further use. Usually this it not necessary for atomic force microscopy but the van der Waals forces between the AFM tip and the gold differ strongly from the forces between the AFM tip and the BCB. This difference disturbs the measurement at the transition between gold and BCB severely, making precise measurements of the gold stripes edges impossible. Therefore the thin gold layer has to be sputtered on top of the structures in order to achieve the same van der Waals force between the surface and the tip throughout the surface, so that a different in the force on the tip is only due to surface features.
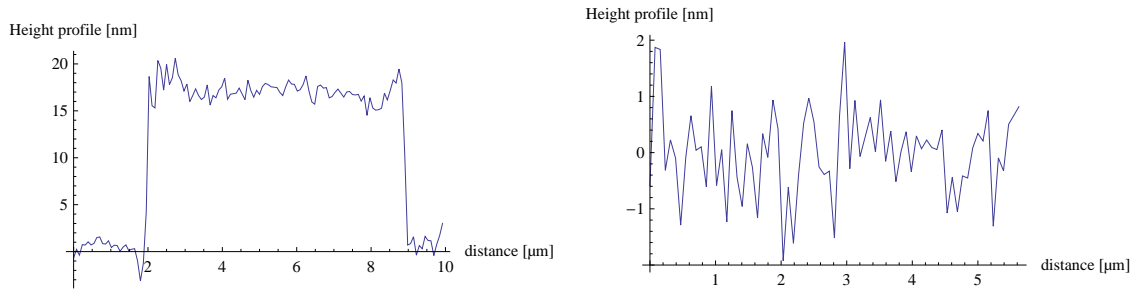
Figure 4.6.: Width and height of the gold stripe measured after lift-off with an AFM after lift-off. Left: profile of the gold stripe Right: roughness of the gold stripes' surface. The designed width of the stripe is 4 µm

Figure 4.5 shows pictures of gold stripes after the lift-off, taken with a scanning electron microscope. A gold stripe with good edge quality can be seen in picture a), whereas the edge quality of the stripes in pictures b) and c) is rather poor. The lift-off for b) and c) was done in an ultrasonic bath and resulted in the flaked edges.

An example for the width and height measurement is seen in figure 4.6. The left plot shows the profile of the stripe, where the width and thickness of the gold stripe can be read off easily to 7 µm and 17 nm, respectively. Note that the nominal stripe width, i.e. the width of the design of the mask, is 4 µm. There are two possible reasons for the fact, that the stripes are wider than the mask. The first explanation is that the lift-off resist and photoresist create an edge bead which leads to a gap between the mask and the resist. Due to diffraction of the ultraviolet light on the small slits of the photomask, the gap results in a wider area exposed to the ultraviolet light. The second reason may be a development time that is picked too long, resulting in dissolution of unexposed photoresist and therefore a widening of the etched stripes in the photoresist.

Upper cladding and top substrate

After the lift-off the gold stripes are covered with another layer of BCB to form the upper cladding. The BCB is applied via spin-coating with a slower spinning speed in order to prevent damage of the gold stripe edges. This second layer has a

Figure 4.7.: Two dies, the left one before the right one after sawing.

thickness of about 35 µm and is soft baked at 100℃ for 60 s. To ensure stability during sawing (see appendix A.1.4) a top substrate (also Schott N-PSK3) is placed on the BCB (after the adhesion promoter for the BCB has been applied).

Hard cure

The hard cure is essentially performed like the soft cure, but at higher temperatures and for a longer time. The oven is set to 230℃ and the dies are baked for 120 minutes. Again the oven is flooded with nitrogen to prevent oxidation of the BCB. During the hard cure the two layers of BCB knit together to from one monolithic layer of fully polymerised BCB. The produced die can be seen in figure 4.7 on the left. The hard cure is the last step performed in the clean room.

Sawing the die into individual wave guides

The dies fabricated in the clean room have the dimensions of 15x15 mm and encapsulate gold stripes of 7 mm length. With an open end diamond wire saw the dies are cut to the appropriate length to form the individual wave guides. The cuts are set perpendicular to the gold stripes, creating wave guides which have a width of 15 mm and a variable length. Cutting this way ensures that every wave guide contains gold stripes of every width.

The diamond wire saw leaves the cutting pressure as a process variable for adjustment via the modification of a balance weight. A high cutting pressure leads to

faster cutting times but rougher facets. Cutting the dies with a low pressure (balance weight 30 g) results in a cutting time of 10 hours to cut through the die once. Increasing the pressure (balance weight 90 g) reduces the cutting time tremendously to about 1 hour, still exhibiting acceptable facet roughness. Thus the counter balance was set to 90 g. Figure 4.7 shows a die before and after sawing.

Polishing the wave guide

After the sawing the facets of the wave guide are too rough to be used right away. In order to perform the coupling in the end-fire scheme (see section 5.1) the LRSPP mode has to be accessible by the excitation beam. Any roughness on wave guide's facet distorts the beam profile, reducing its overlap with the LRSPP mode and with that the coupling efficiency. Therefore smooth facets are required, making the polishing of the wave guide's facets necessary.

The polishing is done on a glass polishing plate with silicon carbide fibre lapping sheets with 5 µm grain size and aluminium oxide fibre lapping sheets with 3, 1 and 0,3 µm grain size. The facets are polished starting with the 5 µm polishing sheet and progressively working it down to the final polish with 0,3 µm grain size. Because of the slightly brittle character of the cured BCB, the polish of the BCB does not reach the quality of the polish of the glass substrate. Figure 4.8 shows wave guides after sawing at the left and the facet of a wave guides after the final polish with 0,3 µm polishing paper at the right.

4.3. Potential improvements to the quality of the plasmonic wave guide

The wave guides fabricated by the manufacturing process described in section 4.2 exhibit the quality necessary for LRSPP propagation. But, of course, there is room to improve the quality of the wave guide. A few measures can be taken that are likely to improve certain aspects of the wave guide:
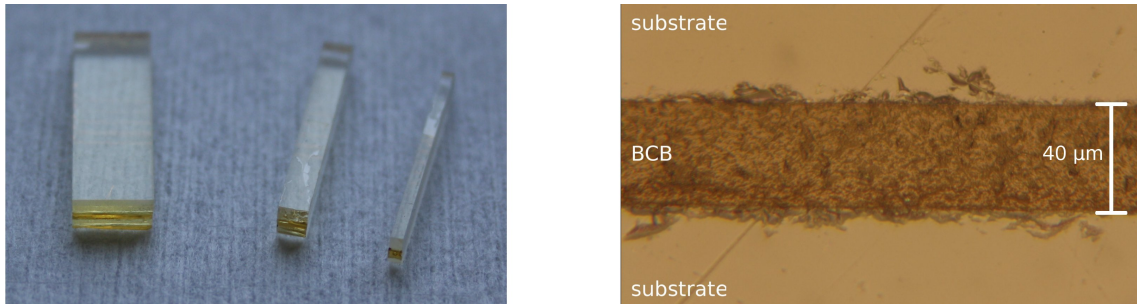
Figure 4.8.: Left: Wave guides of 5, 2 and 1 mm length (from left to right), Right: Microscope picture of a polished wave guide facet

Control of the stripe width

The widths of the gold stripes differ strongly from the corresponding stripe width of the mask. A better control over the stripe width could be achieved if the interplay of the process parameters of the lithography would be improved. This would include new test series with a variation in several photo- and lift-off resist process parameters that have been kept constant during the first tests, for example the resist thickness. An improved control over the stripe width would allow the fabrication of stripes with smaller width.

Adhesion of the gold

A enhancement of the inherently poor adhesion of gold on the BCB would lead to an easier lift-off and an improved edge quality of the gold stripes. A possible measure to increase the adhesion is a short oxygen plasma treatment of the BCB right before the deposition of the gold. The oxygen plasma would activate the uppermost BCB molecules that are then able to bind gold atoms stronger. The downside of such a treatment could be uncontrolled oxidisation of the BCB layer.

Facet polishing

The quality of the facet polish influences the coupling efficiency directly. A smoother polish could be achieved by using diamond polishing sheets instead of aluminium oxide sheets. Diamond polishing sheets mill the glass substrate and the BCB to the
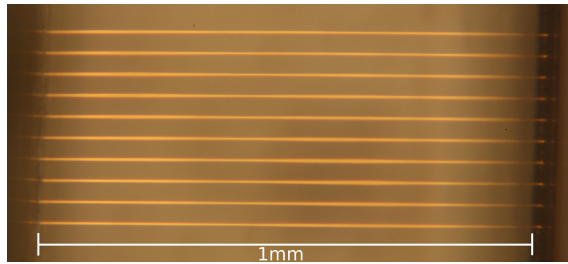
Figure 4.9.: Microscope picture of a finished wave guide. The stripes seen have a
designed width of 4 µm.

same extend and hence prevent scratches in the softer BCB. The scratches occur if
the softer material is carried away faster than the harder one.

All of the above means are likely to improve the quality of different properties of
the wave guide and with that its overall performance, whereas a better polish of the
facets would have the greatest impact on the operation of the wave guide.

4.4. The plasmonic wave guide used in the experiment

With a working fabrication process at hand, a wave guide for experimental use can
be manufactured. A microscope picture of such a wave guide can be seen in figure
4.9. The gold stripes seen have a designed width of 4 µm (the actual width has not
been measured). Even though a wave guide with $l = 1$ mm is shown here, the wave
guide used in the experiment has a length of 3 mm.

In order to fully characterise the plasmonic wave guide used in the experiment, the
width and thickness of its gold stripes have to be measured, because the actual gold
stripe geometry in the wave guide does not agree with the geometry of the pho-
tomask due to fabrication reasons. As mentioned previously, the measurement in
the atomic force microscope can only done if the examined wave guide is sputtered
with gold. Thus the measurements have to be performed on a wave guide different

designed stripe width [μm]	6	4	2	**1,5**	1	0,5
mask stripe width [μm]	6,58	4,35	2,35	**1,85**	1,38	0,832
measured stripe width w [μm]	8,86	7	4,5	**5**	5,51	–
measured stripe thickness t [nm]	17					
measured stripe length l [mm]	3					

Table 4.2.: Measured stripe geometry of the plasmonic wave guide used in the experiment. "designed stripe width" corresponds to the CAD design of the photomask and "mask stripe width" is the actual geometry of the mask. "measured stripe width" refers to the stripe width measured with an AFM on a different die of the same charge. The values for the gold stripe that is used for the LRSPP measurements are printed in bold font.

from the one used in the experiment, but of the same charge and are therefore indirect. The geometry of the gold stripes of the wave guide used in the experiments are shown in table 4.2.

Thus the wave guide for the experiment has been fabricated and fully characterised and is ready to use. Even tough the fabrication process explained here seems fairly straight forward many difficulties had to be overcome to end up with a fully functional LRSPP wave guide. The biggest problems on the way and their solutions are presented in appendix A.1.

5. Experimental setup, measurements and results

In the plasmonic wave guide that has been fabricated, long-range surface plasmon polariton are excited with near-infrared light ($\lambda = 785$ nm) and their propagation is observed. This is achieved by coupling light from a laser diode into a single gold stripe of the wave guide and the LRSPP mode at the end facet of the wave guide is inspected with microscope setup. The coupling sequence of the excitation light in and out of the plasmonic wave guide involves six steps and the coupling into the wave guide is done in the end-fire scheme [17] which will be explained first.

5.1. End-fire coupling

The coupling of the laser beam into the wave guide is done with so called butt-coupling or end-fire coupling [17]. The technique is commonly used in integrated optics and relies on the mode matching of the delivered excitation light and of the wave guide. Thus excitation light with a well defined mode is used, usually from an optical fibre. This mode has to overlap with the mode of the wave guide in order to excite the wave guide's mode. With this scheme coupling efficiencies of 89 % are possible, but as the mode profiles of beams that leave optical fibres are Gaussian, end-fire coupling is only feasible for wave guides with Gaussian-like mode profiles.

This is the reason why the evolution of the mode profile of the long-range surface plasmon polariton into a Gaussian-like shape (see section 2.4.1) is of great experimental importance as it facilitates the excitation of the LRSPP mode tremendously. For plasmonic modes other than the long ranging one, end-fire coupling cannot be
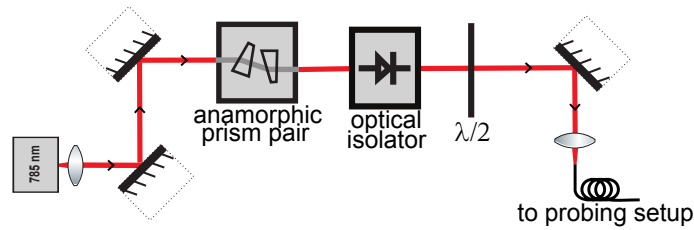
Figure 5.1.: Schematic sketch of the setup's section that is used to create a well
defined light mode

used and thus there are various excitations schemes that all involve additional op-
tical components, like prisms or gratings. In contrary, the end-fire scheme does
without further components.

In practice the optical mode profile of the fibre and with that the profile of the
excitation light is been chosen to match the mode profile of the wave guide. Even
though the matching of the profile can only be optimal for one width (and with that
one mode size) of the wave guide's gold stripes the coupling is still possible for gold
stripes of different width. This is due to the fact, that the LRSPP mode does not
have to overlap with the entire mode of the excitation light, but it is already excited
if the overlap is only partial [17]. In order to perform the coupling, the fibre end is
approached to almost contact the facet of the wave guide. Due to the very small
distance (< 5 µm) between the fibre end and the wave guide, the mode profile of
the excitation light does not change significantly on its way to the facet and the two
modes (excitation light and wave guide) match at the wave guide's facet. This leads
to an efficient coupling without the use of additional optical components.

Furthermore the necessity of the polish of the wave guide's facet becomes obvious.
A rough facet would lead to a distortion in the excitation light's mode, therefore
reducing the overlap between the two modes and with that the coupling efficiency.

5.2. Experimental setup

For the probing of the plasmonic wave guide, the mode of the excitation light has to be well defined. This is achieved by coupling light from a laser in to a polarisation maintaining fibre. As a light source a Sanyo laser diode with an emission wavelength of 785 nm is used. The diode is operated in continuous wave mode and has a maximum output power of 80 mW. In order to realise a circular mode profile to couple into the fibre, the beam passes an anamorphic prism pair. Subsequently, the beam passes through an optical isolator in order to prevent back reflections from the fibre into the diode. With the help of a half wave plate and an aspheric coupling lens (4,6 mm focal length), the light is coupled into a polarisation maintaining fibre. A sketch of this section of the setup can be seen in figure 5.1.

Subsequently, the light that was coupled into the fibre is used to probe the plasmonic wave guide. Light is coupled directly form the fibre into the wave guide and the plasmon mode is observed at the end facet of the wave guide with a microscope setup. Special care has to be taken during the design of the mounts for the fibre end, the wave guide and the microscope objective in order to provide enough degrees of freedom for the coupling, at the same time creating a stable support that prevent vibrations. A schematic sketch and a photograph of the probing part of the setup can be seen in figure 5.2.

In order to probe the plasmonic wave guide, light has to be coupled in and out of it. The three components involved in the coupling are the fibre end for the input coupling, the wave guide and for the output coupling the microscope objective. Out of these three, two components have to be movable in all three directions to be able to perform the coupling at the front and the end facet of the plasmonic wave guide. These spatial degrees of freedom are provided by the fibre end and microscope objective, because the wave guide itself has to be mounted rotatably in order to compensate for misalignments that occur naturally while affixing the wave guide on the sample holder. This arrangement of fibre end, wave guide and microscope objective results in a very flat and versatile setup. Furthermore with the microscope
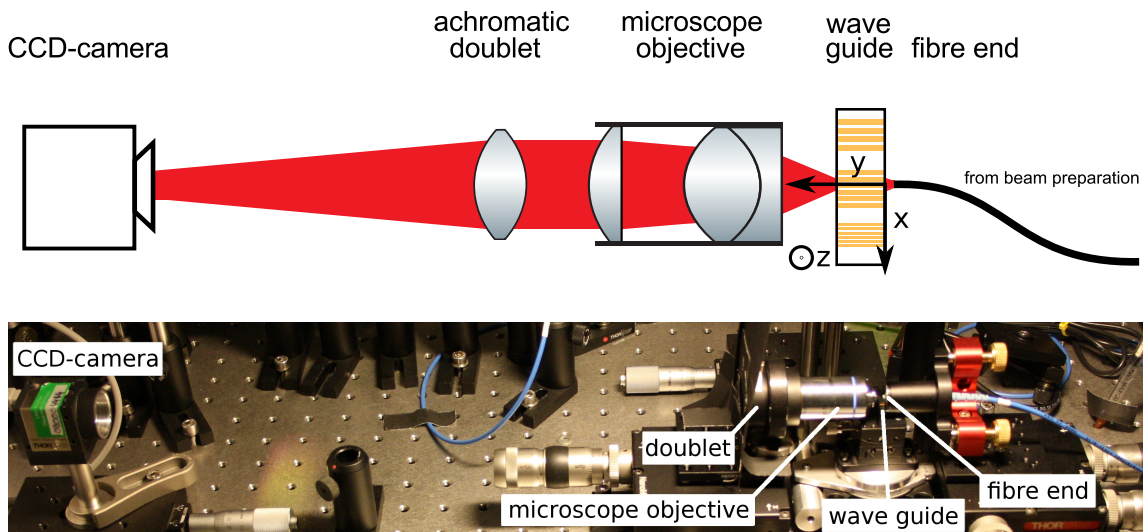
Figure 5.2.: Schematic sketch (top) and photograph (bottom) of the probing part of the setup. The arrangement of the fibre end, wave guide and microscope objective can be seen on the right, the CCD-camera on the left.

objective and fibre end movable the field of view can be changed without changing the coupling into the wave guide and vice versa. A detailed photograph of the arrangement of these three components can be seen in figure 5.3 a).

The fibre end that is used to perform the end-fire coupling is that of a standard terminated fibre with a PC fibre connector. The fibre is mounted in a fibre adapter in a way that a few millimetres of the ferrule protrude from the adapter. The adapter itself is affixed rotatably in a mirror mount on a translation stage in order to allow for the adjustment of the polarisation of the excitation beam, as the light that leaves the fibre is linearly polarised along one of the polarisation maintaining axes of the fibre. The desired direction of the beam's polarisation is in the z-direction (vertically polarised), because the dominant electric field component of the LRSPP mode that has to be excited extends in the z-direction, as explained in section 2.4.1.

As the last step the end facet of the wave guide is examined with a microscope setup to capture the emitted light from the long-range surface plasmon polariton mode.
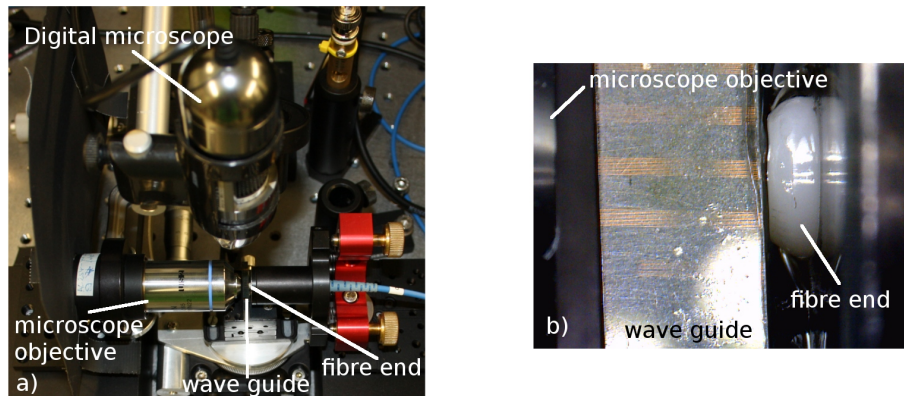
Figure 5.3.: a) Photograph of the fibre end, wave guide and microscope objective arrangement and the digital microscope. b) Picture of the digital microscope taken during alignment.

The microscope objective is an Olympus PlanN 40x objective with a numerical aperture of 0,65 and a working distance of 0,6 mm. It is mounted in a mirror mount on a translation stage in order to bring the wave guide's end facet into the focal plane. Right behind the objective, an achromatic doublet (400 mm focal length) is affixed. It focusses the picture of the objective onto the chip of a CCD-camera (1024x768 pixels) that is positioned in the doublet's focus. With the microscope setup arranged in that way a resolution of 2 µm is achieved. A photograph of the complete probing setup can be seen in figure 5.2, bottom.

5.3. Coupling sequence

The coupling of the excitation light into a single gold stripes of the plasmonic wave guide is a difficult task as the optical access to the front facet of the wave guide is blocked by the fibre end. Even with optical access to the facet (which is the case for the end fact) the adjustment can only be done very roughly as the 15 nm thick gold stripes cannot be seen with optical tools.

In order to ease the adjustment, a simple digital microscope with a maximal magnification of 92x is used. It is mounted directly above the wave guide, allowing to

track the position of the fibre end and the gold stripes on a monitor. This way the fibre end can be adjusted in the x- and y-direction to hit a specific gold stripe, but no information about the height difference (z-direction) between the fibre end and the gold stripe is given. The digital microscope can be found in the detailed photograph of the probing setup (Fig. 5.3 a)) and a picture taken with it during the coupling process can be seen in figure 5.3 b).

5.3.1. Adjustment steps

The adjustment of the fibre end and the microscope objective to the wave guide is done in several steps:

1. Height adjustment of the microscope objective
2. Alignment of the fibre end to the microscope objective
3. Insertion of the wave guide between fibre end and microscope objective
4. Adjustment of the fibre end to excite the LRSPP mode
5. Readjusting the microscope objective
6. Fine tuning of the coupling

Height adjustment of the microscope objective

Initially the height of the microscope objective has to be set to meet the height of the BCB layer of the wave guide. This is done simply by moving the wave guide in front of the microscope objective and adjusting the height until the middle of the BCB layer lies in the centre of the microscope picture.

Alignment of the fibre end to the microscope objective

At this point the wave guide is removed and the fibre end is brought within the working distance of the microscope objective. The fibre end is aligned in a way that its core is centred in the microscope picture.

Insertion of the wave guide between fibre end and microscope objective

The aligned microscope objective and fibre end are then separated by movement in opposite directions along the y-axes and the plasmonic wave guide is reinserted using its translation stage (x-direction). With the use of the digital microscope (mounted above the wave guide), one of the gold stripes is positioned in front of the fibre end.

Adjustment of the fibre end to excite the LRSPP mode

In the next step the coupling of the excitation light into the plasmonic wave guide is done. In order to position the fibre end precisely the translation stage of the fibre end is equipped with piezoelectric actuators, delivering a precision of 5 nm. Furthermore an index matching gel is used between the fibre end and the front facet of the wave guide in order to reduce the effect of the imperfect polish of the front facet. The refractive index of the gel is matched to the refractive index of the fibre core, having the advantage that only one optical interface is encountered by the excitation light at the wave guide's facet (BCB – gel). Moreover the difference of refractive indices at this BCB – gel interface is smaller than that of a BCB – air interface would be without gel. This leads to a smaller refraction of the excitation light at the rough facet surface and thus a better coupling.

Successful coupling shows as a strong reduction of forward scattered light (light which is not coupled from the fibre into the gold stripe), which is picked up by the microscope objective. While moving the wave guide which contains 10 identical stripes at a distance of 30 µm along the x-axis, a reduction in intensity of the scattered light occurs periodically. If this feature is observed, the wave guide is then positioned such that a minimum of forward scattered light is picked up by the microscope objective, thus the light is coupled into the plasmonic wave guide.

Readjusting the microscope objective

In order to observe the plasmonic mode coupled out of the wave guide the microscope objective is realigned because the end of the used gold stripe might be out of sight.
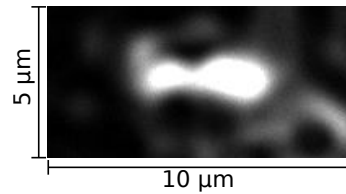
Figure 5.4.: Microscope picture of the plasmon mode at the end facet of the wave guide. [gold stripe dimensions: thickness $t = 17$ nm, width $w = 5$ µm, length $l = 3$ mm]

Fine tuning of the coupling

Finally the coupling into the wave guide can be optimized by fine tuning of the fibre end and the alignment of the wave guide's rotational degrees of freedom. An improvement in the coupling efficiency shows directly as an increase in the intensity of the radiating plasmonic mode.

Having completed these 6 steps, the LRSPP mode found this way can then be further examined.

5.4. Observation of the long-range surface plasmon polariton mode

Figure 5.4 shows the plasmonic mode coupled out of the wave guide, which reconverts into light by the reverse principle of end-fire coupling. Due to the imperfect polishing of the BCB at the end facet (see figure 4.8) imaging errors occur and the mode profile becomes distorted[1].

---

[1]This result represents merely the first observation of the long-range surface plasmon polaritons. Due to the sensitive and time consuming fabrication process and the difficult coupling routine only a single working wave guide could be fabricated and examined within the time limits of this thesis. The first successful detection of a long-range surface plasmon polariton was not accomplished until the very end of the experiment time, thus only qualitative measurements can be presented here. Unfortunately, the time did not permit quantitative measurements or improvements on the wave guide's quality.
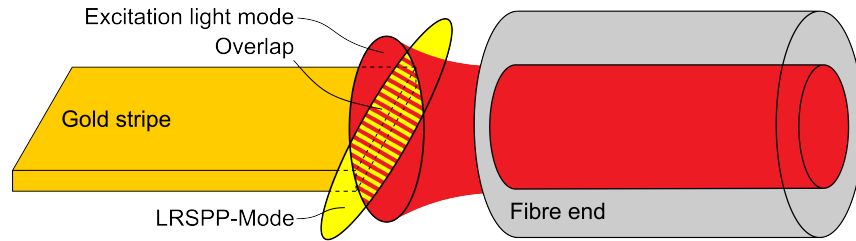
Figure 5.5.: Schematic sketch of the overlap measurement. The overlap of the excitation light mode (red) and of the LRSPP mode (yellow) is illustrated as the hatched area.

Because of the distortion only a first approximation of the size of the plasmonic mode can be given. It is estimated to 4 µm and 2 µm in x- and y-direction, respectively. An important experimental circumstance that shall not go unmentioned is the fact that the LRSPP mode is much brighter than the forward scattered light. This allows a reduction of the sensitivity of the CCD-camera to an extend that only the LRSPP mode is visible.

Even though the size of the LRSPP mode cannot not be determined precisely from the microscope picture, it is possible to derive the mode profile from the overlap of the optical mode of the fibre with the LRSPP mode. This overlap is measurable with high accuracy, because the fibre end can be moved along the front facet of the wave guide very precisely with the piezoelectric actuators of the translation stage (5 nm precision). The profile of the LRSPP mode can then be derived from the overlap, if the mode profile of the excitation light is known. As the overlap is the convolution of the LRSPP mode with the mode of the excitation light (essentially the optical mode of the fibre), deconvolution of the measured overlap with the optical mode profile of the fibre yields the desired LRSPP mode profile. This situation is illustrated schematically in figure 5.5.

In order to determine the overlap, the total intensity of the LRSPP mode is measured as a function of the excitation beam's offset from the coupled position. In order to
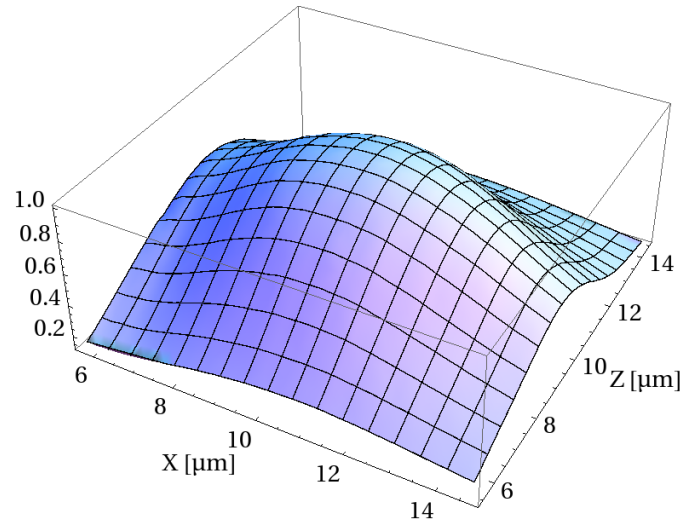
Figure 5.6.: Measured overlap of a Gaussian optical mode from the fibre with the LRSPP mode. The center of the gold stripes cross-section lies at $x = 10$ µm, $y = 10$ µm. [gold stripe dimensions: thickness $t = 17$ nm, width $w = 5$ µm, length $l = 3$ mm]

achieve the offset, the fibre end is gradually misaligned in x- and z-direction. The maximal offset is 5 µm in each direction, where steps of 0,25 µm length are used. This way a 10x10 µm square of the wave guide's front facet is scanned. For each step the total intensity of the LRSPP mode is summed in order to determine the coupling efficiency and with that the overlap between fibre mode and the LRSPP mode.

A plot of the measured overlap can be seen in figure 5.6, where the used gold stripe has thickness $t = 17$ nm, width $w = 5$ µm and length $l = 3$ mm. Unfortunately, the mode could not be derived, because the exact mode profile of the excitation light has yet to be measured. Anyhow, at first sight the measurement supports the estimate of the LRSPP mode profile done previously.

The influence of the distance between fibre end and wave guide facet on the coupling efficiency was examined as well. The overlap measurements have been performed
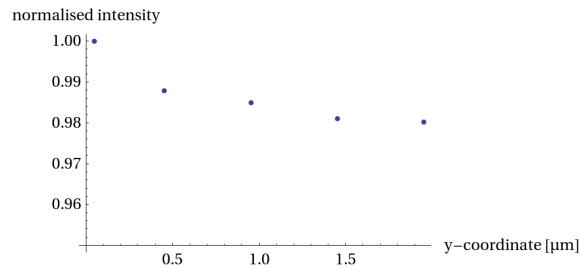
normalised intensity

Figure 5.7.: Plot of the normalised intensity at the brightest spot for different distances between fibre end and wave guide facet.[gold stripe dimensions: thickness $t = 17$ nm, width $w = 5$ µm, length $l = 3$ mm]

for different distances, with a step size of 0,5 µm over a range of 2 µm. From that the influence of the distance on the coupling can be seen. The results can be found in figure 5.7 where the summed intensity at the brightest spot as a function of the distance between the fibre end and the wave guide facet is shown. Clearly, the distance has only a small effect on the coupling efficiency which is not surprising if the Rayleigh length is compared to the propagation distance. As the Rayleigh length of the excitation beam is ~ 140 µm and the travelling distance between fibre end and wave guide facet is 2 µm at the most, the beam widens only insignificantly on its way to the wave guide. Thus the effect of the distance between fibre end and wave guide facet on the overlap, and with that the coupling efficiency, is of lesser importance.

In summary the measurements are very promising and show that the excitation and propagation of long-range surface plasmon polaritons at a free-space wavelength of 785 nm can be achieved. This insight is even more valuable as the attenuation of long-range surface plasmon polaritons at near-infrared frequencies is predicted to be several orders of magnitude higher than at standard telecom wavelength [8].

From a practical point of view the detection of long-range surface plasmon polariton excitations shows that the experimental setup exhibits the usability and the stability necessary to detect and further quantify this interesting phenomenon.

6. Summary and outlook

In this thesis the principle and the fabrication process of a LRSPP wave guide for light of 785 nm wavelength are explained and first measurements on the wave guide were performed. The main part of the work was dedicated to find a suitable design for the wave guide and to realise this design in the challenging microfabrication process.

Within the thesis, the theory of long-range surface plasmon polaritons is displayed and the consequences for the wave guide design are drawn. One of the most important conclusion from the theory lies in the fact, that a difference as small as $3 \cdot 10^{-3}$ in the refractive index of the dielectric above and below the metal stripe would lead to a cut-off of the LRSPP mode. Therefore the wave guide was designed with the same dielectric material above and below the wave guide, following the design of Nikolajsen *et al.* [2].

The fabrication of the wave guide itself is done using photolithography and electron beam evaporation to apply the gold onto the lower dielectric. The process is complicated by the fact that gold has inherently a very poor adhesion on the dielectric as long as no adhesion promoter, like a thin titanium layer, is used. Because any adhesion promoter would disturb the refractive index and the permittivity of the dielectric cladding, it cannot be used without the risk of cutting off the LRSPP mode. In order to avoid the detachment of the weakly bounded gold stripe from the dielectric during the lift-off, a double layer photoresist structure was used. The use of the second layer creates an undercut in the resist faces that define the gold structures for the evaporation. Because of this undercut the evaporated gold on the dielectric has no contact to the gold on the photoresist and therefore the stress on

the gold stripes during lift-off is reduced. This allows the design of gold wave guides without an adhesion promoter.

In the experiment a laser beam of 785 nm wavelength is coupled into a polarisation maintaining fibre in order to create a well defined optical mode. The fibre end is then aligned directly in front of one of the wave guide's gold stripes to perform the coupling in the end-fire scheme [17]. The size of the optical mode in the fibre matches the mode size of the LRSPP. Finally, the light transmitted through the plasmonic wave guide is observed with a microscope setup and a CCD-camera. First measurements clearly show a LRSPP mode escaping the end facet of the plasmonic wave guide. This is believed to be the first observation of a long-range surface plasmon polariton in the near-infrared spectrum.

With this working design and functioning fabrication process for LRSPP wave guides at hand, attenuation, coupling losses, and mode field diameters for various stripe geometries can be determined. As the attenuation of the long-range surface plasmon polariton mode at a wavelength of 785 nm is presumed to be several orders of magnitude higher than at 1,55 µm (where these properties are already measured), these measurements bear attraction in themselves as they are the first examination of a long-range surface plasmon polariton in the near-infrared spectrum.

The next steps would lead to the creation of bent wave guides that shall be used in a further step to build couplers. As LRSPP couplers would merely be beam splitters for the light that has been inserted in the ends, bosonic phenomenons like the Hong-Ou-Mandel effect could be shown, even though the coupling is done through the surface plasmon polaritons, a collective oscillation of fermions.

Another application is collecting the emission of single photons from a nano diamond containing single NV-centres. The underlying idea is that the NV-centre of the diamond nanocrystal couples with the field above the gold stripe and therefore emits a photon in the LRSPP mode. Though in this case, special care has to be taken to assure the matching of the permittivites.

The mentioned applications are just two examples of the possible uses for long-range surface plasmon polaritons. With their successful demonstration at a free-space wavelength of 785 nm, it is shown that long-range surface plasmon polaritons are not limited to telecom wavelength only, but have the potential to become useful tools throughout the optical and infrared spectrum.

A. Appendix

A.1. Difficulties in the fabrication process

The fabrication processes of nanoscale structures are naturally very sensitive and prone to errors. This is especially true if the standard fabrication procedures cannot be used. Usually few nanometres of Titanium are evaporated on the substrate before the deposition of the gold to improve the very poor the adhesion of gold on the substrate. But the titanium layer would create a disturbance in the delicate layer structure needed for long-range surface plasmon polaritons and is therefore not applicable. Hence for the deposition of gold without an adhesion promoter made it necessary to use a double layer resist structure (lift-off resist and photoresist) in order to create an undercut and thus minimize the forces on the evaporated gold during the critical lift-off. The generation of the undercut prove to be a major problem as well as the fabrication of a lower cladding which is plane enough for the 15 nm gold stripe. The missing adhesion promoter complicated the lift-off process as well and unforeseen problems occurred during the sawing of the dies. In total more than 200 substrates have been used and with that more than 200 attempts had to be taken before the first functioning wave guide was fabricated.

A.1.1. Planarisation of the lower BCB layer

The roughness of the surface of the lower cladding is of utter importance concerning the quality of the gold stripe that is to be deposited on top of it. With a gold thickness of only 15 nm the roughness of the lower cladding's surface should be within a few nanometres. Otherwise the gold stripe would become strongly undulated relative to its thickness. The used polymer (BCB, tradename Cyclotene)
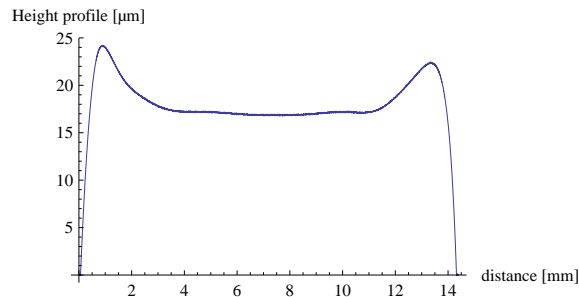
Height profile [µm]

Figure A.1.: Profile of the BCB layer with edge bead after soft cure

exhibits such planarisation abilities by its chemical design but other materials for the cladding had been considered as well (like SiO_2, applied via plasma-enhanced chemical vapour deposition), but had to be discarded due to unsatisfying surface roughnesses [23].

Originally the used BCB creates surfaces of the demanded quality on a microscopic scale, but because of the small substrate size (15x15 mm) — standard wafer sizes in the industry are 51 - 200 cm in diameter — the edge bead creates a bowl on a macroscopic scale. A measured profile of the formed bowl with a depth of about 7 µm can be seen in figure A.1. The edge bead has to be removed because it prevents the resists applied in the next step from spreading equally. This would lead to uncontrollable layer thicknesses of the lift-off resist and photoresist, creating non reproducible results if the lithography would work at all.

Various attempts to remove the edge bead chemically with the solvent for BCB failed. The solvent prove to be too aggressive for the small area of the substrate and attacked most of the BCB on the substrate, resulting in an uneven and rough layer. Approaches to mask the edge of the substrate did not have the desired effect as well.

Finally, the edge bead could be removed by a combination of two means. Firstly a third spinning step is added to the spin routine with the highest possible acceleration for a short time. With that the amount of residual BCB can be reduced without altering the layer thickness significantly. In a second step the remaining edge bead

Parameter	Influence on
lift-off resist: soft bake time	adhesion to BCB, etch rate
lift-off resist: soft bake temperature	adhesion to BCB, etch rate
photoresist: soft bake time	etch rate of exposed regions
photoresist: soft bake temperature	etch rate of exposed regions
exposure time	edge quality, stripe width
developer concentration	etch rate
development time	edge quality, undercut depth

Table A.1.: free process parameter for the creation of the undercut

is removed mechanically with a razor blade. The BCB on the perimeter of the substrate is scratched off right after the spin coating. The combined use of the two techniques creates a profile and surface of the BCB that is suitable for the gold stripe evaporation (see figure 4.2 in on page 35).

A.1.2. Creation of an undercut in the resist layer structure

The creation of an undercut is a very delicate process as it depends on the correct combination of various properties of the used chemicals. These properties are (a) the lift-resist thickness and its etch rate in the developer, (b) the photoresist thickness and the etch rates of its exposed and unexposed regions, (c) the adhesion of the lift-off resist to the BCB, and (d) the exposure and development time. These properties are set by 15 process parameters. In order to simplify the adjustment process the two resists thickness are set constant, reducing the free parameters to 7. An overview of the parameters and its influences gives table A.1.

The tests are done in charges of 6 – 10 substrates, each having the same soft bake parameters for both resists and the exposure time, development time and developer concentration were varied. Every attempt is evaluated under an optical microscope with a magnification up to 500x. Only peculiar substrates were analysed in a scanning electron microscope due to the time-consuming nature of such an examination.

Figure A.2 shows a collection of scanning electron microscope pictures of the double layer resist structure illustrating different attempts to create an undercut. The series of pictures does not show every measure taken but it is used as an example to showcase a few steps on the tedious path to a suitable undercut.

In figure A.2 a) the two layers (lift-off resist and photoresist) can clearly be distinguished, but no undercut can be seen. This was due to the fact that the lift-off resist had a very slow etch rate because the soft bake of the lift-off resist was too hot. The soft bake temperature was lowered from figure A.2 a) to b) and the lift-off resist showed some decomposition at the bottom. Lowering the soft bake temperature even further, the resist separated from the BCB and lost its desired structure (figure A.2 c)). This adhesion problem was due to the lower soft bake temperature of the lift-off resist. Additionally the BCB had not been dehydrated before the application of the resists, which reduced the adhesion even further. The direct processing of the soft cured substrates right from the oven solved the adhesion problems but the undercut did not grow in the extent expected. Prolonging the development time further to about 1 hour, created an undercut, as seen in figure A.2 d), but it also wore out the edges to very shallow slopes. Additionally the lift-off resist did not vanish completely, a faint residue can still be seen on the substrate. In order to shorten the development time the concentration of the developer was increased, leading to higher etch rates. However, the higher concentration did not yield the expected results, as shown in figure A.2 e). The edges grew even worse, becoming almost flat and strongly irregular. Large sections of the photoresist were undermined completely and collapsed as a whole.

A satisfying solution was finally found when the used lift-off resist (LOR 1A) was replaced by the lift-off resist LOR 3B, which has a higher solubility (both sold by Micro Chem Corp). With the experience gathered it took only a few attempts to create the undercut. The etch rate increased tremendously, shortening the development time to 2 minutes. At the same time the soft bake of the resist could be done at 180℃ to ensure the best adhesion. The relatively short development time
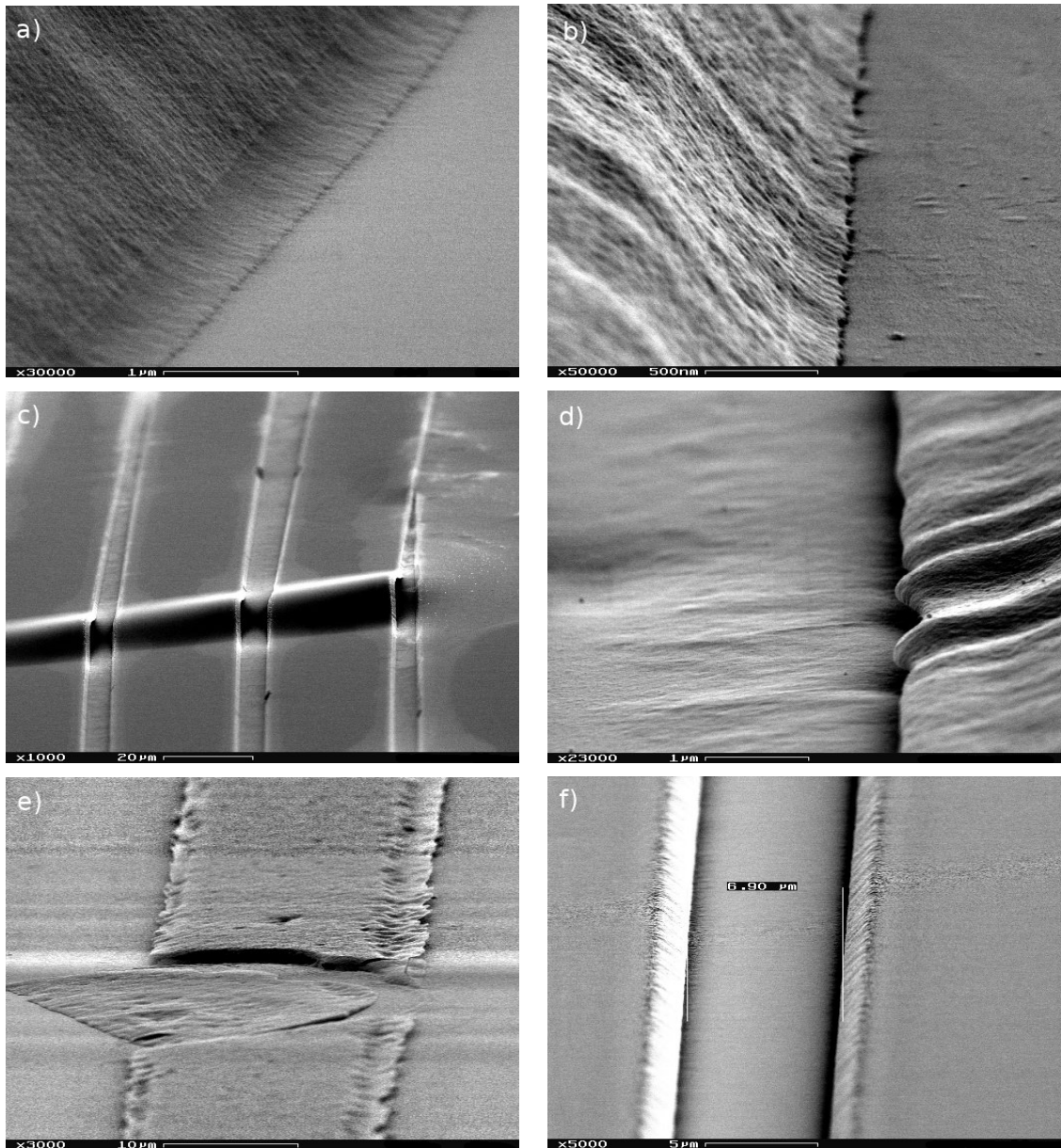
Figure A.2.: Scanning electron microscope pictures of different attempts to create an undercut in the resist structure

spared the edges, leading to steep photoresist faces that are needed for a good lift-off process (figure A.2 f)).

A.1.3. Clean lift-off of the resist structure

The weak adhesion of the gold on the BCB poses difficulties for the lift-off process as well. The gold stripes on the BCB are only loosely bound and rip off very easily, thus every kind of force during the lift-off process has to be minimized. One standard technique — the lift-off in an ultra-sonic bath — can be excluded right away, due to its high mechanical impact.

The gentler standard way suggests the dwelling of the dies in a solvent for several hours. While still in the solvent the residual gold can then be blown away through careful application of air. A pipette is used to create turbulences in the water that remove the unwanted gold residues on the die. In practice even this gentle treatment turns out to be too strenuous for gold structures on BCB. On the one hand, regularly whole stripes rip off, while on the other hand not all of the residual gold could be removed, leading to interconnected gold stripes. Thus this technique leads to unsatisfactory results either.

Again a non standard scheme had to be found. The method that shows consistently the best results comprised of soaking the dies in a solvent, but unlike before the dies are turned upside down. In order to prevent scratching of the gold stripes the dies are placed in a watch glass. This way only the edges of the dies contact the glass and the residual gold can fall to the ground without further treatment.

A.1.4. Sawing of the BCB layer

Major problems did not only occur during the sensitive micromachining steps in the clean room, but also in totally unexpected situations. One of these situations was the sawing of the BCB. The first sawing attempts were made without the additional substrate on top the BCB, but it turned out that it was impossible to saw through the BCB without destroying it. The BCB cracked throughout the whole substrate
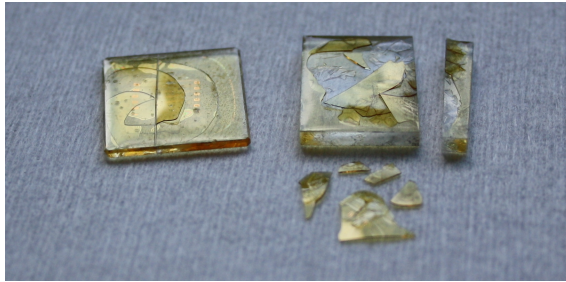
Figure A.3.: Two dies, each with a cracked BCB layer that has been destroyed during sawing

and flaked off in large chunks. A picture of two dies with a destroyed BCB layer can be seen in figure A.3.

The first approach to keep the BCB from cracking was the obvious one: the reduction of the sawing pressure and a decrease in the diamond wire's speed in order to minimise the friction between the wire and the BCB. Except for an increase in cutting time (up to 12 hours for one cut) the attempt did not yield the desired results. The BCB kept cracking sooner or later. Other efforts aimed to increase the adhesion of the BCB to the substrate. The measures ranged from a soft bake of the adhesion promoter prior to the application of the BCB to the deposition of a thin titanium layer on the clean substrates. Nevertheless, none of these measures increased the adhesion sufficiently and thus all of these test layers were destroyed during cutting. The method that enables to saw through the BCB without destroying the layer was the one already explained in section 4.2. Another glass substrate is applied before the hard cure to cover up the bare BCB layer in order to relief the stress on the BCB layer during sawing. Normal coverglasses used in microscopy did not prove sturdy enough to support the BCB layer sufficiently, therefore the 1 mm thick N-PSK3 substrates had to be used to ensure stability. This way the sandwich structure of the wave guide with the BCB layer in between two glass substrates was introduced to cut the dies into the individual wave guides.

Bibliography

[1] Robert Charbonneau, Pierre Berini, Ezio Berolo, and Ewa Lisicka-Shrzek. Experimental observation of plasmon polariton waves supported by a thin metal film of finite width. *Opt. Lett.*, 25(11):844–846, Jun 2000.

[2] Thomas Nikolajsen, Kristjan Leosson, Ildar Salakhutdinov, and Sergey I. Bozhevolnyi. Polymer-based surface-plasmon-polariton stripe waveguides at telecommunication wavelengths. *Applied Physics Letters*, 82(5):668–670, 2003.

[3] Suntak Park, Jung Jin Ju, Jin Tae Kim, Min su Kim, Seung Koo Park, Jong-Moo Lee, Wook-Jae Lee, and Myung-Hyun Lee. Sub-db/cm propagation loss in silver stripe waveguides. *Opt. Express*, 17(2):697–702, Jan 2009.

[4] Alexandra Boltasseva, Thomas Nikolajsen, Kristjan Leosson, Kasper Kjaer, Morten S. Larsen, and Sergey I. Bozhevolnyi. Integrated optical components utilizing long-range surface plasmon polaritons. *J. Lightwave Technol.*, 23(1):413, Jan 2005.

[5] Sergey I. Bozhevolnyi. *Nanophotonics with Surface Plasmons (Advances in Nano-Optics and Nano-Photonics)*. Elsevier B. V., 2007. Chap. 1.

[6] Lukas Novotny and Bert Hecht. *Principles of Nano-Optics*. Cambridge University Press, 2006. Chap. 12.

[7] J. R. Sambles, G. W. Bradbery, and Fuzi Yang. Optical excitation of surface plasmons: An introduction. *Contemporary Physics*, 32(3):173–183, 1991.

[8] Pierre Berini. Plasmon-polariton waves guided by thin lossy metal films of finite width: Bound modes of symmetric structures. *Phys. Rev. B*, 61(15):10484–10503, Apr 2000.

[9] Neil W. Ashcroft and David N. Mermin. *Solid State Physics*. Thomson Learning, Toronto, 1 edition, January 1976.

[10] W. Demtröder. *Experimentalphysik 2: Elektrizität und Optik (Springer-Lehrbuch)* . Springer, 3 edition, 2004.

[11] Takayuki Okamoto. Near-field spectral analysis of metallic beads. In Satoshi Kawata, editor, *Near-Field Optics and Surface Plasmon Polaritons*, volume 81 of *Topics in Applied Physics*, pages 97–123. Springer Berlin / Heidelberg, 2001.

[12] P. B. Johnson and R. W. Christy. Optical constants of the noble metals. *Phys. Rev. B*, 6(12):4370–4379, Dec 1972.

[13] U. Schröder. Der Einfluss dünner metallischer Deckschichten auf die Dispersion von Oberflächenplasmaschwingungen in Gold- Silber- Schichtsystemen. *Surface Science*, 102(1):118 – 130, 1981.

[14] M. Fukui, V. C. Y. So, and R. Normandin. Lifetimes of surface plasmons in thin silver films. *physica status solidi (b)*, 91(1):K61–K64, 1979.

[15] J. J. Burke, G. I. Stegeman, and T. Tamir. Surface-polariton-like waves guided by thin, lossy metal films. *Phys. Rev. B*, 33(8):5186–5201, Apr 1986.

[16] B. Prade, J. Y. Vinet, and A. Mysyrowicz. Guided optical waves in planar heterostructures with negative dielectric constant. *Phys. Rev. B*, 44(24):13556–13572, Dec 1991.

[17] G. I. Stegeman, R. F. Wallis, and A. A. Maradudin. Excitation of surface polaritons by end-fire coupling. *Opt. Lett.*, 8(7):386–388, Jul 1983.

[18] Ian Breukelaar and Pierre Berini. Long-range surface plasmon polariton mode cutoff and radiation in slab waveguides. *J. Opt. Soc. Am. A*, 23(8):1971–1977, Aug 2006.

[19] Pierre Berini. Long-range surface plasmon-polariton waveguides in silica. *Journal of Applied Physics*, 102(5):053105, 2007.

[20] MicroChem, 1254 Chestnut Street, Newton, MA 02464, USA. *LOR Lift-Off Resists*, 2001.

[21] measurement on the soft cured layers were performed by Scott Kisting, engineer at The Dow Chemical Company.

[22] Rohm and Haas Company, Philadelphia, PA, USA. *Microposit S1800 G2 Series Photoresists for microlithography applications.*

[23] material tests done by Marion Kraus in 2009.